Master's thesis

NTNU
Norwegian University of Science and Technology
Faculty of Information Technology and Electrical Engineering
Department of Engineering Cybernetics

Truls Mentzoni Skoglund

Longitudinal Moving Mass Actuation of Fixed-Wing Unmanned Aerial Vehicle (UAV)

Master's thesis in Industrial Cybernetics
Supervisor: Morten Dinhoff Pedersen
June 2021

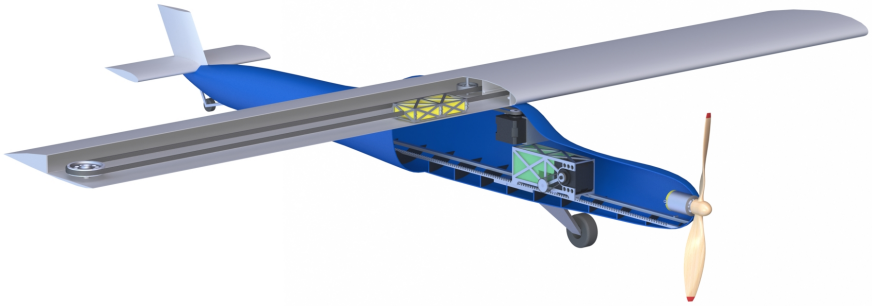

NTNU
Norwegian University of
Science and Technology

Truls Mentzoni Skoglund

Longitudinal Moving Mass Actuation of Fixed-Wing Unmanned Aerial Vehicle (UAV)

Master's thesis in Industrial Cybernetics
Supervisor: Morten Dinhoff Pedersen
June 2021

Norwegian University of Science and Technology
Faculty of Information Technology and Electrical Engineering
Department of Engineering Cybernetics

NTNU

Kunnskap for ei betre verd

Dedicated to my much-beloved grandfather Knut Mentzoni, who has been a source of inspiration

Summary

Moving mass actuation is a control mechanism replacing aerodynamic control surfaces, such as aileron, elevator, and rudder for an airplane by utilizing the motion of internal mobile masses to change the center of gravity. The method allows a more protected system and reduces drag and lift loss since conventional control surfaces create drag when deflected. Control surfaces cannot generate sufficient control moments at high altitudes, due to low air density, and low-speed ranges. Moving mass has great potential because it does not depend on these factors. This thesis presents a UAV design with moving mass control (MMC) and analytic derivation of the non-linear longitudinally equation of motion. The design is carried out in SolidWorks, and simulation is conducted in the MATLAB and Simulink framework. The design presents some design considerations regarding MMC and how the inertia tensor changes depending on the moving mass location. The non-linear model is linearized at trim values enabling the use of linear control theory. The thesis compares two individual control methods; successive loop closure (SLC) and Linear Quadratic Regulator (LQR). Total control of the UAV was achieved for a given ascend/descend and altitude hold reference at a cruise speed of 10 m/s for both control methods. The LQR controller had better stability performance than SLC, but SLC is more robust for step responses. 60 grams is the lowest weight for the moving mass element to control the UAV.

Sammendrag

Bevegelig masseforflytting er en kontrollmekanisme som erstatter aerodynamiske kontrollflater, som høyde-, balanse- og sideror for et fly ved å bruke interne mobile masser til å endre tyngdepunktet. Metoden muliggjør et mer beskyttet system som reduserer vindmotstand og tap av løftekraft siden konvensjonelle kontrollflater skaper luftmotstand når de er avbøyd. Kontrollflater kan ikke skape tilstrekkelige kontrollmomenter ved store høyder, siden lufttettheten er lav, samt ved lave hastigheter. Her har bevegelig massestyring et stort potensial på grunn av at det ikke avhenger av disse faktorene. Denne oppgaven presenterer et UAV design med bevegelig massekontroll og en analytisk utledning av de ikke-lineære langsgående bevegelseslikningene. UAVen er designet i SolidWorks, og simuleringene er gjort i MATLAB og Simulink-rammeverket. Designet viser noen designhensyn med bevegelig massekontroll og undersøker hvordan treghetsmomentet endres med hensyn til plassering av den flyttbare massen. Den ikke-lineære modellen er linearisert ved likevektspunter for å kunne ta i bruk lineær kontrollteori. Oppgaven sammenligner henholdsvis to individuelle kontrollmetoder; *successive loop closure* (SLC) og *Linear Quadratic Regulator* (LQR). Full kontroll av UAV ble oppnådd med en referanse for stigning/synking og konstant høyde ved en cruisehastighet på 10 m/s for begge kontrollmetodene. LQR-kontrolleren hadde bedre stabilitetsegenskaper enn SLC, men SLC er mer robust for stegresponser. 60 gram er den laveste vekten til den bevegelige massen for å kontrollere UAVen.

Preface

This master thesis concludes the author's two-year master's degree in Industrial Cybernetics at the Norwegian University of Science and Technology (NTNU). The author has a background in Mechanical Engineering. Being able to draw knowledge and experience from both fields into product development and design has been one of the primary motivations for the degree. I want to thank my supervisor Morten Dinhoff Pedersen for our weekly meetings with general discussion, guidance throughout this thesis, and his practical way of teaching and for making the theory easily accessible.

Table of Contents

List of Tables

List of Figures

Chapter 1

Introduction

For most aircraft, the aerodynamic control surfaces are aileron, elevator and rudder. The control surfaces create a moment for controlling the aircraft motion in pitch, roll and yaw, illustrated in figure 1.1. A deflected control surface increases the drag and reduces the lift force. Moving mass control (MMC) introduces an alternative aircraft control mechanism by changing the UAV's center of gravity and eliminating drag increase and lift loss. Also, MMC is often installed inside the vehicle and thereby not exposed to icing or erosion like conventional control surfaces. These two factors are the primary justifications for investigating the potential for moving mass actuation.

Due to the lack of practical design considerations for moving mass actuation in literature, this thesis presents a UAV design with MMC and elaboration on the following objectives:

- A historical background of MCC, with literature review
- Describing essential performance criteria for a stable UAV and necessary control theory
- Deriving the longitudinal equations of motion for a UAV
- Making computer-aided design (CAD) of UAV with moving mass actuation
- Designing and tuning two different controllers for comparison

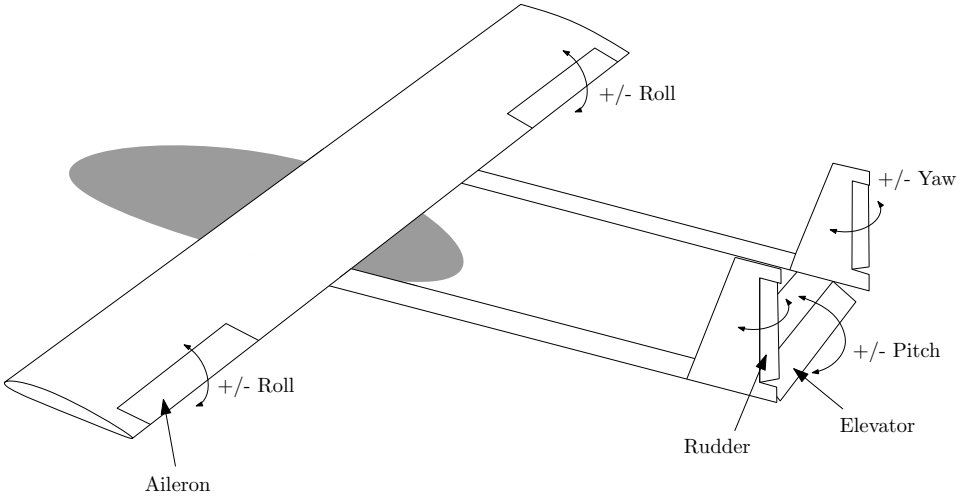

Figure 1.1: Airplane with conventional control surfaces to adjust pitch, roll and yaw [1]

Chapter 2

Pre-study

This chapter starts with a historical perspective on MMC and a further definition of a UAV and the challenges related to icing on aircraft surfaces. Finally, a section on MMC as addressed in the literature is included.

2.1 History

Moving mass actuation has roots back to the late 1800s, where Lilienthal shifted his body to move CG to control his monoplane glider ”Normalsegelapparat”,[2].

The British and French engineers met a considerable problem when developing and designing the Concorde in the 1960s. For aircraft flying at supersonic speed, the lift force will move backward and generate an arm from the center of gravity (CG), creating a pitch moment acting on the aircraft. The pilot must use the elevator to compensate for this moment, and the air resistance and fuel consumption increase significantly. The only mass that can shift during flight is fuel. By implementing valves and pumps, fuel could circulate according to needs between the front and back of the plane. Consequently, the center of gravity is moved backward and the plane is kept horizontal without elevator input,[3]. This fuel transfer system is implemented in many commercial aircrafts today.

2.2 Fixed-Wing Unmanned Aerial Vehicle (UAV)

A UAV is an airborne vehicle without a human pilot onboard and can either be controlled remotely or autonomously. Fixed-wing configuration entails planes equipped with wings that generate lift produced by the plane’s forward airspeed and the shape of the wings. On rotating wing aircrafts, the rotating blades connected to a vertical axis creates the lift.

Today, unmanned aircraft is part of the modern military worldwide. These range from unmanned aircraft (e.g., Wasp, Black Hornet Nano and Nighthawk) to larger vehicles

(e.g.,Global Hawk, Predator) for numerous applications, including reconnaissance, surveillance, battle damage assessment, and communication relays,[4].

Civil and commercial applications are not as common as military use. However, there is potential in several industries, including environmental monitoring (e.g., pollution, weather and scientific applications), forest fire monitoring, homeland security, border patrol, drug interdiction, aerial surveillance and mapping, traffic monitoring, precision agriculture, disaster relief, ad hoc communications networks, rural search and rescue, [4]. UAVs recently played a central search and rescue role in the dramatic and tragic landslide disaster in Gjerdrum in Norway. The UAVs task was to locate survivors using its thermal cameras in an avalanche area where it was too dangerous for humans and rescue dogs to enter, [5].

2.3 Icing

There is a potential risk of icing on aircraft surfaces when flying in cold climate conditions. For light aircraft, the added mass of the accreted ice can be catastrophic. Icing can increase drag, decrease lift and lead to less maneuverability of the plane. The main types of ice are glaze, also known as clear icing, and rime. Both are illustrated in figure 2.1. Glaze icing can be almost transparent and has a smooth surface compared to rime which is brittle and opaque. Glaze icing may be more problematic than rime due to accumulation over a larger area of the airframe and onto unprotected areas, [6], like servos for managing control surfaces. A third type of icing worth mentioning is water droplets flowing towards the control surfaces at the rear of the wings, [7]. The wing's aerodynamic characteristics may change due to the build-up of icing and thereby modify the pressure distribution around control surfaces and lead to uncommanded control deflections, [8]. Moving mass actuation can potentially make UAVs more resistant to icing, where the control mechanism is inside the airplane and not exposed like control surfaces. Additionally, ice accretion may change the center of gravity, and MMC enables continuous adjustments of the center of gravity to compensate for the weight of ice deposits.

2.4 Literature Review

Moving mass actuation occupies much of the designated space for people and cargo and is therefore unfitted for transport airplanes. Consequently, the control mechanism is better suited for unmanned aerial vehicles (UAV). Moving mass control is also highly coupled and has nonlinear dynamics, [10]. Furthermore, the servo forces moving the mass element can affect the vehicle's translation and rotation motion, [11]. The moving mass will also change the inertia tensor and affect the dynamic response of the system, [12].

Moving mass actuation has been widely explored as a control mechanism in literature. This control method is explored for airplanes, satellites, underwaters and reentry vehicles, to mention some applications. In hypersonic flight, aerodynamic control surfaces are subjected to surface ablation and erosion, possibly resulting in blocked steering gears, [13]. Furthermore, the control surface's efficiency decreases with higher altitude as the

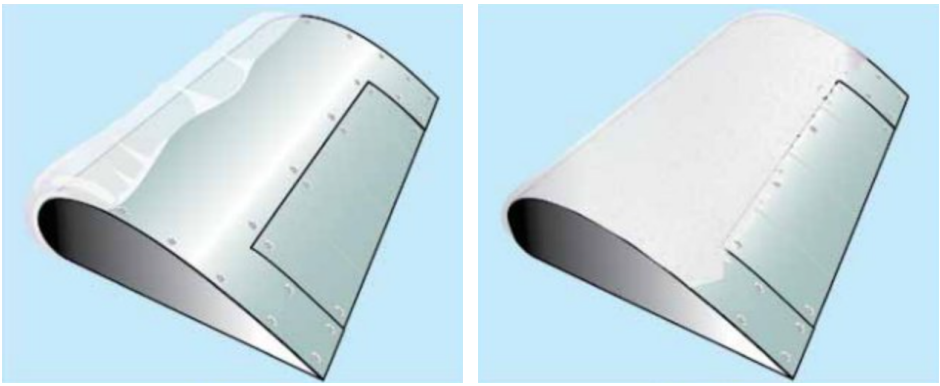

(a) Glaze or clear ice **(b)** Rime ice

Figure 2.1: Illustration of glaze and rime icing on an airfoil, [9]

density of air becomes lower, [14]. For example, the density and pressure at 30 km are only 1.8% and 1.1% of the corresponding sea-level values, [15]. Therefore, mass-actuation has a unique advantage for near-space vehicles and is suited for attitude control in high altitudes.

Wang et al. (2020)[16] proposed moving mass control of a low-speed high altitude long endurance (HALE) airplane with flexible wings, illustrated in figure 2.2. The UAV has two individual moving masses within the wings, rather than conventional ailerons for controlling roll motion. The results showed that the moving mass could improve rolling moment with the inherent large span of HALE vehicles. Under nominal flight conditions, the UAV is operating at 20 km altitude with a flight speed of 25 m/s.

Erturk (2016)[17] studied moving mass control for UAV and based the equation of motion from a study by Waishek et al. (2009)[18]. Who examine the dynamic equations for a receiver aircraft in aerial refueling. Erturk compared UAV with three different control actuations: (1) only conventional control surface actuation as in figure 1.1, (2) mass-actuated with a mass moving longitudinally located in the fuselage for controlling pitch and a lateral mobile mass within the wings for roll control. Finally, (3) same as (2) but supplemented with a rudder for controlling yaw. The comparison showed that the second and third alternatives could reduce propeller torque and the load on the engine, due to the

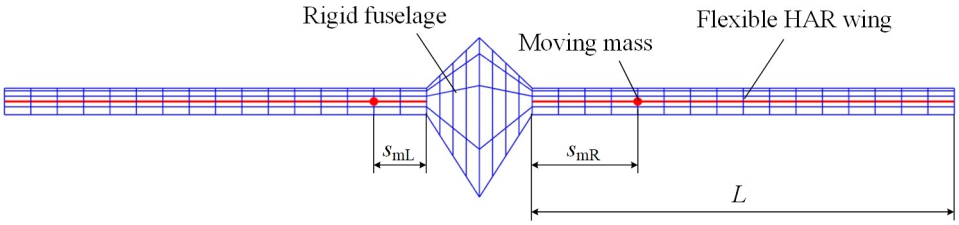

Figure 2.2: Schematic of HALE aircraft with moving mass control [16]

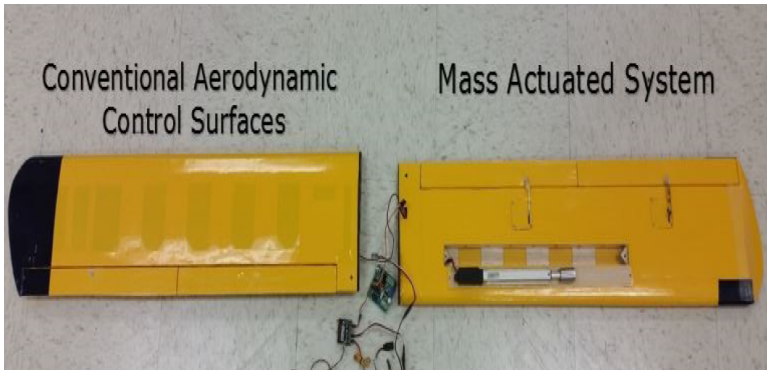

Figure 2.3: Design of wing with linear actuators from the study by Vengate[19]

reduced drag by removing ordinary control surfaces. Thus, increased range and endurance. Furthermore, it was concluded that mass-actuation has similar or better controllability in the lower speed range. In contrast, aerodynamic actuation is better for high speeds. Moreover, control configuration number (2) could not perform coordinate turns[1] with zero sideslip angle due to no actuation provide yawing moment. Erturk suggested using one motor mounted on each wing to create differential thrust and cope with the lack of yaw control when only MMC is utilized.

In collaboration with Vengate (2016)[19], they presented an actual flight with a test airplane equipped with a linear actuator placed inside both wings for controlling roll, see figure 2.3. During the test flight, the UAV was brought to steady level flight with conventional control surfaces. They deactivated the aileron servos at a safe altitude, switched to mass-actuation, and put the UAV in a steady turn. The flight demonstrated how mass-actuation could be utilized instead of conventional control surfaces like ailerons.

2.4.1 Moving Mass Control Examples

In a study of Chen et al. (2012)[20] a stratospheric airship[2] with several control methods; conventional aerodynamics control surfaces, vector thrust, ballonet, and moving mass were examined. One of the moving masses moved longitudinally to control the pitch angle and a lateral mass controlled roll angle, see figure 2.4. The study showed that the moving mass control ability is unaffected by the airship's airspeed. Hence, moving mass control is better than control surfaces at low speeds.

Haus et al. (2016)[22] present a concept and design for a large quadrotor with MMC capable of lifting over 50 kg by using combustion engines to give the necessary lift and endurance. A traditional quadrotor changes attitude by adjusting the thrust in the motor. Combustion engines do not have the same instant response as electric propulsion systems.

[1] There is no lateral acceleration, which is more comfortable for the passengers while turning since their weight acts downward and into their seats.

[2] Stratospheric airship operates at 20 km and is used for environmental monitoring, emergency rescue and civil communication, [21]

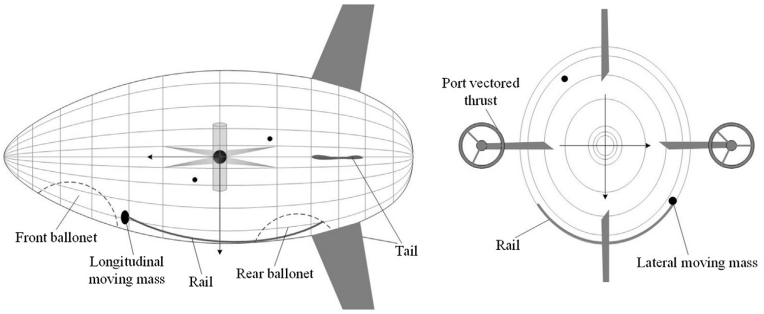

Figure 2.4: Airship with moving masses [20]

Therefore, it might be difficult to stabilize a quadrotor in flight with differential thrust from combustion engines. Haus et al. (2016)[22] proposed to use four moving masses placed in the four arms of the quadrotor, seen in figure 2.5a, to change the center of gravity for controlling pitch and roll movement. At the same time, the combustion engines perform yaw and height control.

Moving mass control is advantageous for underwater vehicles because the joint to the rudder surface can corrode in seawater. Also, at low velocities, the efficiency of the rudder is poor. Figure 2.5b illustrates an underwater vehicle equipped with a moving mass actuator by Graver (2005),[23]. Here two moving masses control pitch and roll, whereas a variable ballast mass control depth.

Regarding spacecraft, the purpose of moving mass control can be to stabilize or control the vehicle's behavior. At low orbital altitudes, lower than approximately 450 km, spacecraft suffers attitude disturbance from the aerodynamic forces, [25]. To counteract these disturbances, moving mass actuation can create momentum to stabilize the spacecraft. Virgilli-Llop et al. (2019)[25] found that changing the spacecraft's center of mass position is a viable method to counteract disturbances. Spacecraft can also suffer from wobbling, meaning its axis of maximum moment of inertia is not aligned with the moment of momentum vector, [24]. A report by Childs (1972)[24], convey observations that movement from the astronauts (moving mass) inside the space station was the primary source for wobble motion. Therefore, Dr. Eugene Worley suggested using moving mass actuation to generate torque for eliminating wobble motion and reduce attitude oscillations. As a result, Child designed a single moving mass placed tangential to the space station moving along a tube, see figure 2.5c.

Docking[3] and reentry[4] of spaceships is dangerous for astronauts, particularly if the angular velocity is large. Also, uncontrolled rotation may be hazardous and can occur as a result of an accident like collisions. Edvards and Kaplan (1974)[26] propose to use a moving mass control to transform rotation motion into a simple spin with a movable mass parallel to the spinning axis. At the same time, the despinning could be performed by

[3]Process of joining two space vehicles
[4]Spacecraft move from outer space into the atmosphere

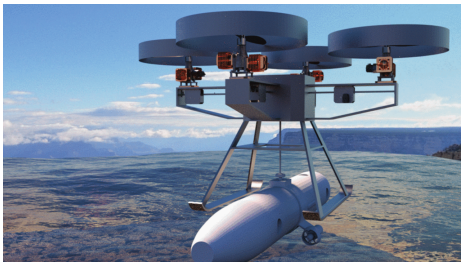

(a) Quadrotor with MMC [22]

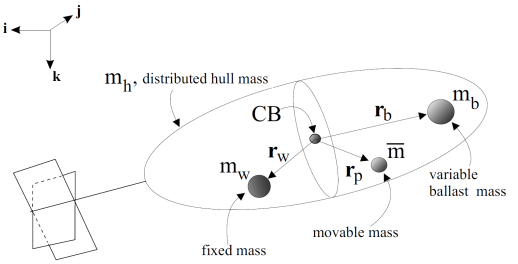

(b) Underwater vehicle with MMC [23]

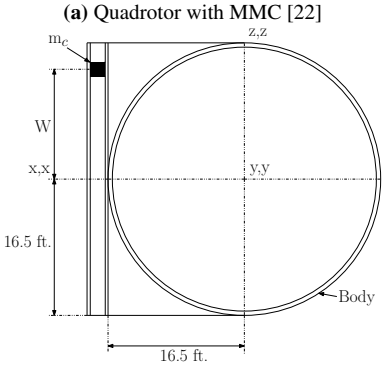

(c) MMC as stabiliser configuration for space station [24]

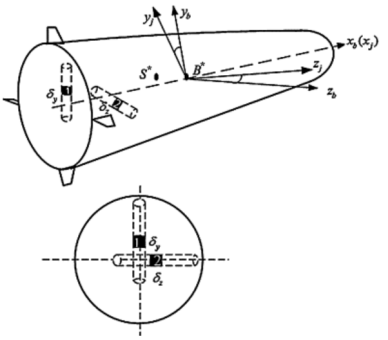

(d) Reentry vehicle with MMC and ailerons [11]

Figure 2.5: Different vehicles with moving mass actuation

another control system, like thrust. Their simulation shows that a movable mass with 1% of the space station's total weight can stabilize the uncontrolled rotation in 2 hours.

Rudder control can be insufficient due to the low density of the upper atmosphere. Moving mass actuation can reduce the aerodynamic thermal load on large velocities and solve the problem with rudder surface damage, [27]. Since the mid-1990s, moving mass actuation has been utilized for controlling reentry vehicles, [21]. Gao et al. (2013) [11] studied the combination of using MMC and ailerons as seen in figure 2.5d. By moving masses along two orthogonal rails, pitch and yaw channel tracking control could be achieved, whereas ailerons control the roll channel. The paper proved advantages in combing these control methods.

Chapter 3

Theory

The stability of a UAV is essential for flight characteristics and is described in this chapter. Furthermore, an explanation of a stable wing design configuration and characterization of different stability responses are given. Finally, two control methods are described: Successive loop closure (SLC) and the Linear Quadratic Regulator (LQR).

3.1 Longitudinal stability

Three primary factors determine the longitudinal stability: the center of gravity's location, and the location and design of the main and tail wing. Figure 3.1 shows a UAV with stable wing configuration. The UAV is pivoting around the center of gravity, and all forces act around it. The main wing is located slightly behind the CG and generates a lift component, creating a moment, causing the UAV to pitch downwards without a counteracting force. Therefore, a horizontal stabilizer is located at the rear of the plane to create a downward force. The tail wing is located farther from the CG and therefore does not need to be of the same magnitude to create a necessary counteracting moment. It is desirable to have a tail wing configuration that creates a restoring force which brings the UAV back to its original position. The restoring force changes with the UAV pitch angle, and there are mainly two factors that influence this: How downwash from the main wing acts on the tail wing and the orientation of the tail wing.

If the UAV is designed with a conventional tail configuration, the air that passes the main wing will deflect downwards, hit the top of the tail wing, and produce downward pressure. The pressure will depend on airspeed, meaning that the UAV will gain airspeed if the UAV pitches down, which increases the downward pressure, creating a moment that pitches the aircraft upwards. The opposite happens when the nose points upward, i.e., reduced airspeed and decreased downward pressure from the tail; consequently, the UAV's weight will overcome the tail moment and move the nose down again. This periodic flight behavior is seen in figure 3.2b and determines whether the UAV has positive, neutral, or negative dynamic stability depending on the UAV response of a disturbance.

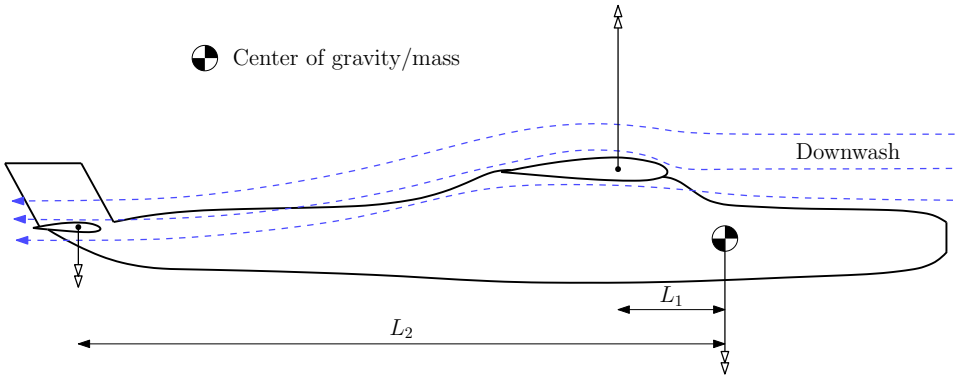

Figure 3.1: Stable wing design configuration

The orientation of the tail wing is the second factor to influence stability. The angle of attack for a tilted tail wing changes based on whether the UAV pitches up or down. If the nose is pointing upward and the horizontal stabilizer has a negative angle of attack, the angle of attack for UAV decreases, and downforce decreases. As a result, the weight of the nose will pull the UAV down.

There are two general types of stability for a UAV; static and dynamic. Static stability is the UAVs ability to return to its original flight attitude after a disturbance. Figure 3.2a illustrates positive, neutral and negative static stability. Positive means that the UAV will return to its original attitude; neutral is the tendency to remain at a constant new attitude after a disturbance, while negative is a progressing deviation from the original position. A UAV left to its own devices flying in a straight level flight will return to a straight level flight even when it is knocked out of direction with positive static stability. This makes it much safer to fly without constantly adjusting the control surfaces to balance the plane. A conventional airplane is designed with static stability. Dynamic determines the behavior of the airframe when subjected to disturbance over time and defined as either; positive, neutral, and negative, as seen in figure 3.2b. Static stability is necessary for the airplane to be dynamically stable. Positive dynamic stability means oscillations are damped over time, neutral is when the oscillations never are damped, whereas negative is growing oscillations.

The dynamic stability can be found by computing the eigenvalues of the coefficient matrix A using:

$$|\lambda \boldsymbol{I} - \boldsymbol{A}| = 0 \tag{3.1}$$

The UAV is dynamically stable if all the eigenvalues of matrix A are located on the left side of the s-plane diagram, illustrated in figure 3.3. By expanding the determinant, the fourth-degree polynomial is given by:

$$\lambda^4 + a_1\lambda^3 + a_2\lambda^2 + a_3\lambda + a_1 = 0 \tag{3.2}$$

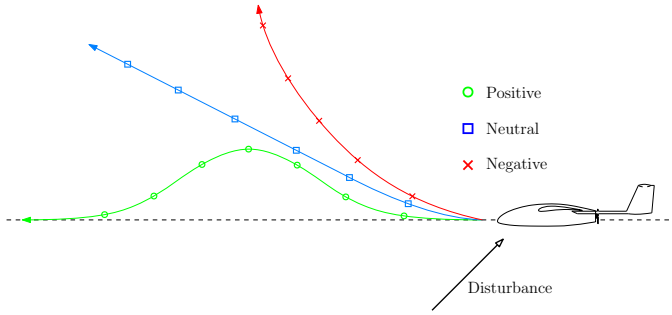

(a) Static stability

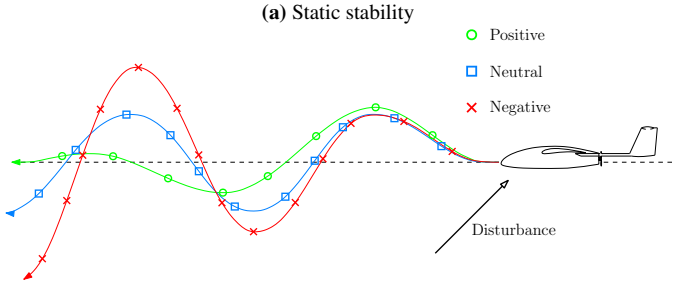

(b) Dynamic stability

Figure 3.2: Static and dynamic stability

This can be factorized into:

$$(\lambda^2 + 2\zeta_{ph}\omega_{ph}\lambda + \omega_{ph}^2)(\lambda^2 + 2\zeta_{sp}\omega_{sp}\lambda + \omega_{sp}^2) \tag{3.3}$$

where the subscript *ph* and *sp* are denoted for the phugoid and short-period modes, respectively. Figure 3.3 typically shows the placement of these modes for different airplanes. The phugoid mode is characterized as a long period oscillation with low damping and can, in some cases, be placed on the right-handed side plane as seen in figure 3.3. Here the mode is unstable, and the oscillation will increase with time. The short-period mode is rapid and usually well damped, with the natural frequency ω_{sp} and relative damping factor ζ_{sp}

Aircraft at speeds close to one Mach yields two real phugoid modes, where one is negative (stable), and one is positive (unstable). The positive mode is referred to as the *tuck mode* since the aircraft's nose is pointing down(*tucking under*) with increasing speed. This is the phenomenon described earlier that the British and French engineers faced when designing the Concorde.

The eigenvalue location denoted □ in figure 3.3 is aircraft with a third oscillatory mode and is typical for fighter aircrafts where the center of gravity often lies aft of the aerodynamic center. As a result, every root of equation 3.3 will become real. If the center of gravity is moved further back, one real root from phugoid and one from short-period mode will merge into a new complex conjugated pair and form the so-called third oscillatory mode. That mode constitutes the major impact on the aircraft's dynamic response controlled by a

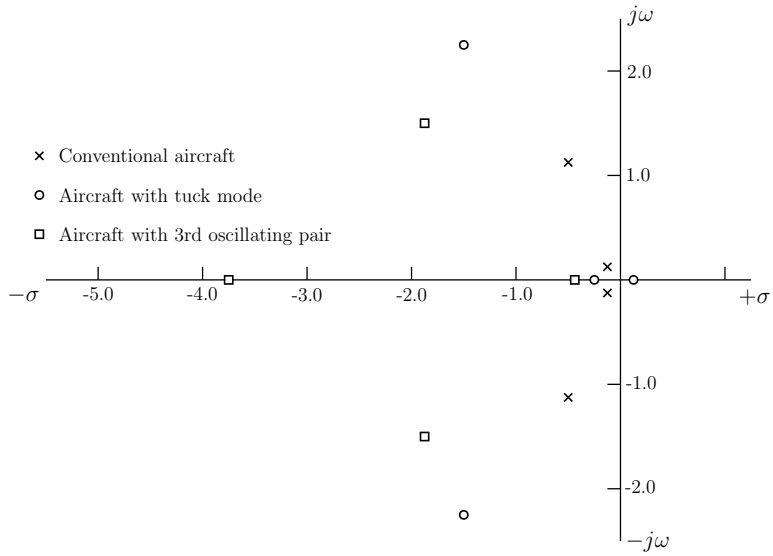

Figure 3.3: Longitudinal eigenvalue plotted in the s-plane diagram,[28]

pilot or automatic control system. One of the real eigenvalues can become positive, leading to dynamic instability. However, for fighter jets, where speed and maneuverability are essential, a slightly unstable aircraft can be preferred because the energy input needed to change the aircraft's attitude is low.

3.2 Control Theory

The dynamics of the UAV is highly coupled and nonlinear, as section 4.4 describes, and therefore it can be challenging to design a robust controller. A robust controller means a system capable of handling uncertainty either in the model or a disturbance like wind. Therefore, controllers are often designed to assume decoupled dynamics, yielding sufficient performance,[4]. The longitudinal dynamics (forward and downward speed, pitching, climbing/descending motion) are decoupled from the lateral dynamics (sideways speed, rolling, and yawing motion). Besides, most flight maneuvers are linearized about trim conditions. This simplifies the equations and dynamics significantly and makes the design of a controller more manageable. Now, linear system theory can be used instead of nonlinear theory. However, global stability cannot be guaranteed.

Several control strategies are relevant for an autopilot design; successive loop closure or Linear Quadratic Regulator (LQR).

Successive loop closure

Successive loop closure, also called cascade loop or nested loop, is a control method with several closed feedback loops, illustrated in figure 3.4 A), instead of designing a single

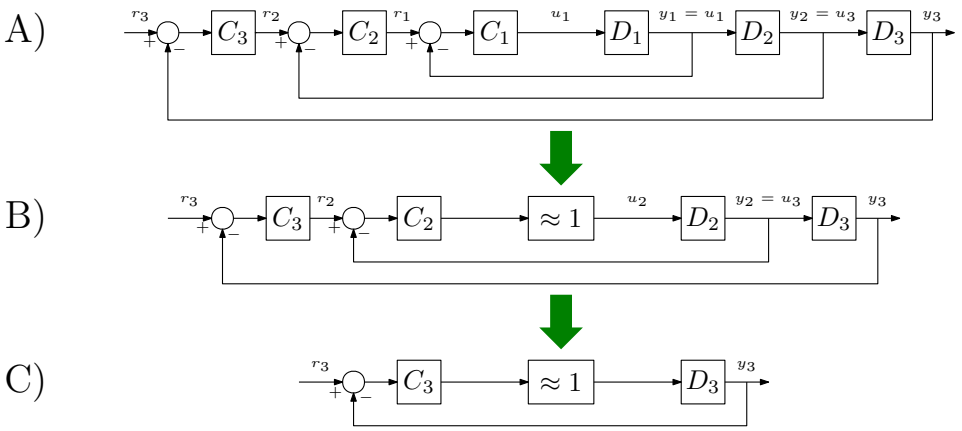

Figure 3.4: Successive Loop Closure, [4]

control system with one single feedback. Let three smaller closed-loop systems describe ascend/descend and altitude hold dynamics to a UAV. D_1 describes the dynamics of a servo/motor controlling elevator or a moving mass longitudinally, D_2 is the dynamic of pitch angle concerning input from the elevator or MMC. Finally, D_3 describes the relation between pitch angle and altitude dynamics. The idea is to close each closed-loop system in succession, where the inner loop has five to ten times higher bandwidth than the next closed-loop system. By letting the inner loop act faster than the outer loop, the outer loop can be tuned on the assumption that the inner loop can be modeled as a gain of one, see figure 3.4 B and C. By this approach, the controllers C_1, C_2 and C_3 can be tuned separately. With successive loop closure, it can be easier to isolate problems in the system and add saturation to the individual inputs. Where r_1 limits max voltage drawn from the battery, r_2 limits movable range on the moving mass, and r_3 sets a constraint on max/min pitch angle on the UAV. Also, cascaded loops increase stability for the system, with the motor controller responding fast to local disturbances, whereas the altitude controller can be tuned more conservatively to reject sensor noise and only respond to relatively slow disturbances like wind gusts.

The controllers C_1, C_2 and C_3 can be Proportional-Integral-Derivative (PID) controllers and the output of a PID controller is:

$$u = k_p e + k_i \int e\, dt + k_d \frac{de}{dt} \tag{3.4}$$

where $e = r - y$ is the error difference between reference and actual output. The proportional gain k_p multiples with the error and makes the plant reacting faster and result in a higher overshoot. Also, a higher k_p will reduce the steady-state error, but not eliminate it. Introducing integral k_i allows the controller to use past information about the deviation from the reference. If the steady-state error is persistent, the integrator repeatedly sums up the input signal and drives the error down. If the plant's actuators are saturated, the integrator may suffer from integral windup, causing low-frequency oscillations in the plant

Table 3.1: Effect of independent P, I and D tuning, [29]

Closed-loop response	Rise time	Overshoot	Settling time	Steady-state error	Stability
Increasing k_p	Decrease	Increase	Small increase	Decrease	Degrade
Increasing k_i	Small decrease	Increase	Increase	Large decrease	Degrade
Increasing k_d	Small decrease	Decrease	Decrease	Minor change	Improve

and lead to instability. Therefore, it is common to add an anti-windup schematic to turn off the integrator when the actuators are saturated. The derivative term k_d is keeping track of the error rate change. Thus, the control input becomes significant if the error rate increases, although the magnitude of the error is relatively small. The derivative adds damping into the system and thereby decreases overshoot. The table 3.1 summarizes the effect of tuning the different coefficients independently.

Linear Quadratic Regulator (LQR)

LQR is a method for finding optimal gains as feedback in a closed-loop system and is based on well-known state-space representation:

$$\dot{\mathbf{x}} = \mathbf{A}\mathbf{x} + \mathbf{B}\mathbf{u} \tag{3.5a}$$

$$\mathbf{y} = \mathbf{C}\mathbf{x} + \mathbf{D}\mathbf{u} \tag{3.5b}$$

The goal is to obtain an optimal control input, u, stabilizing the system. Set of linear equation describe the dynamics of the UAV, and a quadratic cost function given from optimal control theory is given by:

$$J = \int_0^\infty (\mathbf{x}^\top \mathbf{Q}\mathbf{x} + \mathbf{u}^\top \mathbf{R}\mathbf{u})dt \tag{3.6}$$

where $\mathbf{Q}$ is a non-negative definite weighting matrix that penalizes deviation from the actual state and reference value. R is a positive definite weighting matrix that penalizes the consumption of input u. The objective is to minimize the cost function, yielding an optimal control law:

$$u = -\mathbf{K}x \tag{3.7}$$

where the feedback gain $\mathbf{K}$ matrix is found by

$$\mathbf{K} = \mathbf{R}^{-1}\mathbf{B}^\top \mathbf{P} \tag{3.8}$$

The covariance matrix $\mathbf{P}$ is calculated by solving the algebraic Riccati equation:

$$\mathbf{A}^\top \mathbf{P} + \mathbf{P}\mathbf{A} - \mathbf{P}\mathbf{B}\mathbf{R}^{-1}\mathbf{B}^\top \mathbf{P} + \mathbf{Q} = \mathbf{0} \tag{3.9}$$

The equation 3.9 is quadratic, and there may be several solutions to this equation, but only one solution is positive semidefinite. LQR has good stability properties and suits very well for multi-input-multi-output (MIMO) systems. However, the LQR is not guaranteed to be stable when saturating inputs. Integral terms can be introduced for improving the tracking performance for selected states.

Chapter 4

Equation of Motion

This chapter contains the mathematical derivation of the forces acting on the UAV. The equation and syntax are based on literature by Beard and McLain (2012)[4], Fossen (2011)[30] and Fossen(2021)[31]. The UAV is assumed to be rigid and elastic effects can be neglected. Several coordinate systems and 12 state variables must be defined to fully describe the dynamic behavior of the UAV. The 12 state variables can be divided into kinematics and dynamics. Then the longitudinal model for aerodynamics, moving mass, and propulsion is presented.

4.1 Reference Frames

NED, $\mathcal{F}^i$
It is commonly known as North East Down (NED) and is tangential to the earth's surface at a defined home location. The north direction is the inertial x-direction, the east is the

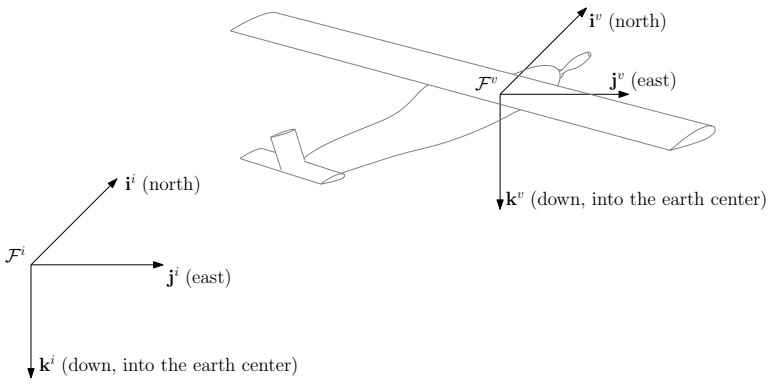

Figure 4.1: The NED and vehicle coordinate frame

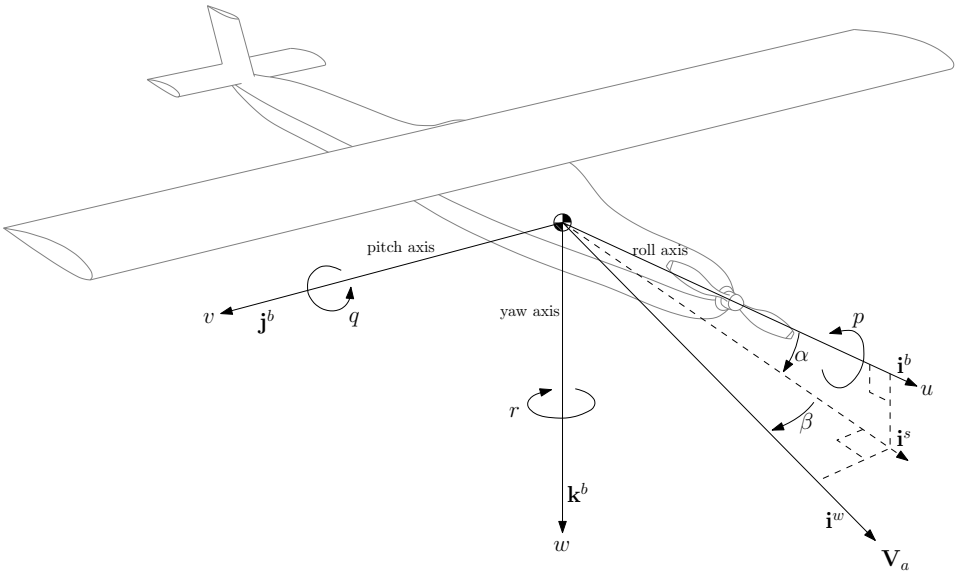

Figure 4.2: States definition with stability and wind frame

y-direction, and the down is referred to as the z-direction. The NED is, in general, not inertial due to the rotation and velocity of the earth. However, it is reasonable to define NED inertial in many applications, giving a reasonable estimate without notable error.

Vehicle, $\mathcal{F}^v$
The origin of the vehicle frame is located in the mass center of the UAV but does not rotate. Meaning the axis of the $\mathcal{F}^v$ is aligned with the axis of the NED frame, and there is only a translation between those coordinate frames.

Body, $\mathcal{F}^b$
The aerodynamic forces and moments are most easily described in the body coordinate frame. The origin is located at the center of mass with the $\mathbf{i}^b$ aligned along the longitudinal body of the vehicle, $\mathbf{j}^b$ points along the right-wing and $\mathbf{k}^b$ points out of the floor in the UAV. By defining the Euler angles Θ: roll(ϕ), pitch(θ) and yaw(ψ), the rotation and motion can be denoted in the vehicle frame and can be expressed in the body frame by using the following rotation matrix:

$$\begin{aligned}\mathcal{R}_v^b &= \begin{bmatrix}1 & 0 & 0\\ 0 & \cos(\phi) & \sin(\phi)\\ 0 & -\sin(\phi) & \cos(\phi)\end{bmatrix}\begin{bmatrix}\cos(\theta) & 0 & -\sin(\theta)\\ 0 & 1 & 0\\ \sin(\theta) & 0 & \cos(\theta)\end{bmatrix}\begin{bmatrix}\cos(\psi) & \sin(\psi) & 0\\ -\sin(\psi) & \cos(\psi) & 0\\ 0 & 0 & 1\end{bmatrix}\\ &= \begin{bmatrix}c_\theta c_\psi & c_\theta s_\psi & -s_\theta\\ s_\phi s_\theta c_\psi - c_\phi s_\psi & s_\phi s_\theta s_\psi + c_\phi c_\psi & s_\phi c_\theta\\ c_\phi s_\theta c_\psi + s_\phi s_\psi & c_\phi s_\theta s_\psi - s_\phi c_\psi & c_\phi c_\theta\end{bmatrix}\end{aligned} \tag{4.1}$$

$$\mathcal{R}_b^v = (\mathcal{R}_v^b)^T = \begin{bmatrix} c_\theta c_\psi & s_\phi s_\theta c_\psi - c_\phi s_\psi & c_\phi s_\theta c_\psi + s_\phi s_\psi \\ c_\theta s_\psi & s_\phi s_\theta s_\psi + c_\phi c_\psi & c_\phi s_\theta s_\psi - s_\phi c_\psi \\ -s_\theta & s_\phi c_\theta & c_\phi c_\theta \end{bmatrix} \tag{4.2}$$

where $c_\theta := \cos(\theta)$ and $s_\psi := \sin(\psi)$. The Euler angles is an intuitive representation, but pitch angle θ is singular at ± 90 degrees. It is also, known as a gimbal lock, but is not a concern for less maneuverable UAVs.

Stability and wind frame, $\mathcal{F}^s$ and $\mathcal{F}^w$
The airplane's velocity relative to the surrounding is denoted as V_a, and is generally not aligned with the body axis. V_a is decomposed into $\mathcal{F}^s$ with the *angle of attack* α and into the $\mathcal{F}^w$ with *sideslip angle* β. The angles are defined with the following rotation matrix:

$$\mathcal{R}_b^s(\alpha) = \begin{bmatrix} \cos(\alpha) & 0 & -\sin(\alpha) \\ 0 & 1 & 0 \\ \sin(\alpha) & 0 & \cos(\alpha) \end{bmatrix} \tag{4.3a}$$

$$\mathcal{R}_s^w(\beta) = \begin{bmatrix} \cos(\beta) & \sin(\beta) & 0 \\ -\sin(\beta) & \cos(\beta) & 0 \\ 0 & 0 & 1 \end{bmatrix} \tag{4.3b}$$

The aerodynamic forces and moments originate in the wind frame and are transformed into the body frame with the following rotation matrix:

$$\mathcal{R}_w^b(\alpha, \beta) = (\mathcal{R}_b^w(\alpha, \beta))^T = (\mathcal{R}_s^w(\beta) \cdot \mathcal{R}_b^s(\alpha))^T \tag{4.4}$$

The airspeed vector in the body frame can be expressed in terms of angle of attack, sideslip angle, and magnitude as

$$\boldsymbol{V}_a^b = \begin{bmatrix} u_r \\ v_r \\ w_r \end{bmatrix} = \mathcal{R}_w^b \cdot \begin{bmatrix} V_a \\ 0 \\ 0 \end{bmatrix} = V_a \cdot \begin{bmatrix} \cos(\alpha)\cos(\beta) \\ \sin(\beta) \\ \sin(\alpha)\cos(\beta) \end{bmatrix} \tag{4.5}$$

Inverting this relationship results in

$$\begin{aligned} V_a &= \sqrt{u_r^2 + v_r^2 + w_r^2} \\ \alpha &= \tan^{-1}\left(\frac{w_r}{u_r}\right) \\ \beta &= \sin^{-1}\left(\frac{v_r}{V_a}\right) \end{aligned} \tag{4.6}$$

4.2 State Variables

12 state variables are necessary to describe the full kinematics and dynamics of a UAV. Those states can be expressed in a vectorial setting according to Fossen(2011)[30]:

$$\text{NED position } \boldsymbol{p}_{nb}^{n} = \begin{bmatrix} x^n \\ y^n \\ z^n \end{bmatrix} = \begin{bmatrix} \text{North} \\ \text{East} \\ \text{Down} \end{bmatrix}$$

$$\text{Attitude } \boldsymbol{\Theta}_{nb} = \begin{bmatrix} \phi \\ \theta \\ \psi \end{bmatrix} = \begin{bmatrix} \text{Roll} \\ \text{Pitch} \\ \text{Yaw} \end{bmatrix}$$

$$\text{Linear velocity } \boldsymbol{v}_{nb}^{b} = \begin{bmatrix} u \\ v \\ w \end{bmatrix} = \begin{bmatrix} \text{Forward velocity} \\ \text{Sideway velocity} \\ \text{Vertical velocity} \end{bmatrix}$$

$$\text{Angular velocity } \boldsymbol{\omega}_{nb}^{b} = \begin{bmatrix} p \\ q \\ r \end{bmatrix} = \begin{bmatrix} \text{Roll rate} \\ \text{Pitch rate} \\ \text{Yaw rate} \end{bmatrix}$$

with the forces and moment in body denoted as:

$$\text{Body-fixed force } \boldsymbol{f}_{b}^{b} = \begin{bmatrix} X \\ Y \\ Z \end{bmatrix} = \begin{bmatrix} \text{Drag} \\ \text{Side force} \\ \text{Lift} \end{bmatrix}$$

$$\text{Body-fixed moment } \boldsymbol{m}_{b}^{b} = \begin{bmatrix} L \\ M \\ N \end{bmatrix} = \begin{bmatrix} \text{Rolling moment} \\ \text{Pitching moment} \\ \text{Yawing moment} \end{bmatrix}$$

The velocity vector $\boldsymbol{v}_{nb}^{b}$ is transformed from body to NED by

$$\dot{\boldsymbol{p}}_{nb}^{n} = \mathcal{R}_{b}^{v}(\boldsymbol{\Theta}_{nb}) \cdot \boldsymbol{v}_{nb}^{b} \tag{4.7}$$

Equally, the angular velocity vector $\boldsymbol{\omega}_{nb}^{b}$ and $\boldsymbol{\Theta}_{nb}$ is related through a transformation matrix $\boldsymbol{T}(\boldsymbol{\Theta}_{nb})$ according to

$$\dot{\boldsymbol{\Theta}}_{nb} = \boldsymbol{T}(\boldsymbol{\Theta}_{nb}) \cdot \boldsymbol{\omega}_{nb}^{b} \tag{4.8}$$

where

$$\boldsymbol{T}(\boldsymbol{\Theta}_{nb}) = \begin{bmatrix} 1 & \sin(\phi)\tan(\theta) & \cos(\phi)\tan(\theta) \\ 0 & \cos(\phi) & -\sin(\phi) \\ 0 & \frac{\sin(\phi)}{\cos(\theta)} & \frac{\cos(\phi)}{\cos(\theta)} \end{bmatrix} \tag{4.9}$$

4.3 Kinematics

The kinematics defines the relation between positions and velocities without regarding forces and moments causing the motion. The six degrees of freedom(DOF) kinematic equation for the airframe can be denoted in a matrix-vector form

$$\dot{\boldsymbol{\eta}} = \boldsymbol{J}_{\boldsymbol{\Theta}}(\boldsymbol{\eta}) \cdot \boldsymbol{\nu}$$
$$\begin{bmatrix} \dot{\boldsymbol{p}}_{nb}^{n} \\ \dot{\boldsymbol{\Theta}}_{nb} \end{bmatrix} = \begin{bmatrix} \mathcal{R}_{b}^{v}(\Theta) & \boldsymbol{0}_{3\times3} \\ \boldsymbol{0}_{3\times3} & \boldsymbol{T}(\boldsymbol{\Theta}_{nb}) \end{bmatrix} \cdot \begin{bmatrix} \boldsymbol{v}_{nb}^{b} \\ \boldsymbol{\omega}_{nb}^{b} \end{bmatrix} \tag{4.10}$$

4.4 Dynamics

The relation between forces and moments and the moment is called the dynamics. For a general body, six DOF nonlinear dynamic equation is given by:

$$\boldsymbol{M}\dot{\boldsymbol{\nu}} + \boldsymbol{C}(\boldsymbol{\nu})\boldsymbol{\nu} + \boldsymbol{D}(\boldsymbol{\nu})\boldsymbol{\nu} = \boldsymbol{\tau} + \boldsymbol{g}(\boldsymbol{\eta}) + \boldsymbol{g}_0 + \boldsymbol{w} \tag{4.11}$$

where

$$\boldsymbol{\eta} = \begin{bmatrix} \boldsymbol{p}_{nb}^n \\ \boldsymbol{\Theta}_{nb} \end{bmatrix} = \begin{bmatrix} x^n \\ y^n \\ z^n, -h \\ \phi \\ \theta \\ \psi \end{bmatrix} \qquad \boldsymbol{\nu} = \begin{bmatrix} \boldsymbol{v}_{nb}^b \\ \boldsymbol{\omega}_{nb}^b \end{bmatrix} = \begin{bmatrix} u \\ v \\ w \\ p \\ q \\ r \end{bmatrix}$$

and
$\boldsymbol{M}$ - Inertia matrix with added mass
$\boldsymbol{C}(\boldsymbol{\nu})$ - Coriolis-centripetal matrix included added mass
$\boldsymbol{D}(\boldsymbol{\nu})$ - Damping matrix
$\boldsymbol{g}(\boldsymbol{\eta})$ - Gravitational force vector
$\boldsymbol{g}_0$ - Vector used for pretrimming
$\boldsymbol{\tau}$ - Control input and aerodynamic forces (thrust, moving mass or aerodynamic control surface input)
$\boldsymbol{w}$ - Disturbance vector for wind

Added mass is neglected due to the low density for air compared to marine crafts where water has much higher density and plays a significant role. Also, damping and g_0 can be disregarded, leading to the following expression:

$$\boldsymbol{M}_{RB}\dot{\boldsymbol{\nu}} + \boldsymbol{C}_{RB}(\boldsymbol{\nu})\boldsymbol{\nu} = \boldsymbol{\tau}_{RB} + \boldsymbol{g}(\boldsymbol{\eta}) + \boldsymbol{w} \tag{4.12}$$

Where

$$M_{RB} = \begin{bmatrix} m\boldsymbol{I}_3 & \boldsymbol{0}_{3\times3} \\ \boldsymbol{0}_{3\times3} & \boldsymbol{I}_{CG} \end{bmatrix}, \quad C_{RB} = \begin{bmatrix} m\boldsymbol{S}(\boldsymbol{\omega}_{nb}^b) & \boldsymbol{0}_{3\times3} \\ \boldsymbol{0}_{3\times3} & -\boldsymbol{S}(\boldsymbol{I}_{CG}\boldsymbol{\omega}_{nb}^b) \end{bmatrix} \tag{4.13}$$

$\boldsymbol{S}(x)$ is the skew symmetric matrix for calculate the cross-product according to:

$$\boldsymbol{\epsilon} \times \boldsymbol{a} := \boldsymbol{S}(\boldsymbol{\epsilon}) \cdot \boldsymbol{a} \tag{4.14}$$

Where

$$\boldsymbol{S}(\boldsymbol{\epsilon}) = -\boldsymbol{S}^{\mathrm{T}}(\boldsymbol{\epsilon}) = \begin{bmatrix} 0 & -\epsilon_3 & \epsilon_2 \\ \epsilon_3 & 0 & -\epsilon_1 \\ -\epsilon_2 & \epsilon_1 & 0 \end{bmatrix}, \qquad \boldsymbol{\epsilon} = \begin{bmatrix} \epsilon_1 \\ \epsilon_2 \\ \epsilon_3 \end{bmatrix} \tag{4.15}$$

The inertia tensor $\boldsymbol{I}_{CG}$ is defined as

$$\boldsymbol{I}_{CG} := \begin{bmatrix} I_{xx} & -I_{xy} & -I_{xz} \\ -I_{yx} & I_{yy} & -I_{yz} \\ -I_{zx} & -I_{zy} & I_{zz} \end{bmatrix} \tag{4.16}$$

For symmetric body about the xz plane, the $I_{xy} = I_{yz} = I_{yx} = I_{zy} = 0$. This is a reasonable assumption for conventionally UAVs with control surfaces mechanism. However, the inertia tensor will change for moving mass actuated UAVs, but the effect on the dynamics is small, as described in section 4.5. The restoring terms are obtained by solving the triple integrals:

$$I_{xx} = \int_V (y^2 + z^2)\rho_m dV \tag{4.17a}$$

$$I_{yy} = \int_V (x^2 + z^2)\rho_m dV \tag{4.17b}$$

$$I_{zz} = \int_V (x^2 + y^2)\rho_m dV \tag{4.17c}$$

$$I_{xz} = I_{zx} = \int_V xz\ \rho_m dV \tag{4.17d}$$

These terms are often calculated with a CAD software.

The gravitational force is proportional to the UAV‘s mass and acts at the center of gravity and is denoted in the vehicle frame, $\mathcal{F}^v$. The gravity force is transformed into the body frame, $\mathcal{F}^b$ by

$$g_{\text{ijk}}(\eta) = \mathcal{R}_v^b \cdot \begin{bmatrix} 0 \\ 0 \\ mg \end{bmatrix} = \begin{bmatrix} -mg\ \sin(\theta) \\ mg\ \cos(\theta)\ \sin(\phi) \\ mg\ \cos(\theta)\ \cos(\phi) \end{bmatrix} \tag{4.18}$$

The gravity force produces no moments since the force act through the center of gravity. The total gravitation term then becomes

$$g(\eta) = \begin{bmatrix} -mg\ \sin(\theta) \\ mg\ \cos(\theta)\ \sin(\phi) \\ mg\ \cos(\theta)\ \cos(\phi) \\ 0 \\ 0 \\ 0 \end{bmatrix} \tag{4.19}$$

τ_{RB} includes the aerodynamics forces propagated from the wings, propulsion forces, and moment created by moving mass mechanism in the following formula:

$$\boldsymbol{\tau}_{RB} = \boldsymbol{\tau}_{\text{aero}} + \boldsymbol{\tau}_{\text{prop}} + \boldsymbol{\tau}_{\text{mass}} \tag{4.20}$$

The equation 4.12 is highly nonlinear and coupled. Therefore, it is common to divided motion into longitudinal and lateral motion where longitudinal motion depends on axial force (X), the normal force (Z), and the pitching moment (M). In contrast to lateral motion that depends on side force (Y), rolling moment (L), and yawing moment(N).

4.5 Longitudinal Motion

The airfoil creates a pressure distribution and can be modeled by a lift force, a drag force, and a moment, illustrated in figure 4.3. The forces are applied at the aerodynamic center, also known as a quarter-chord point,[4] and are given by:

$$\begin{aligned} F_{\text{lift}} &= \frac{1}{2}\rho \boldsymbol{V}_{\text{wing}}^2 S C_L(\alpha) \\ F_{\text{drag}} &= \frac{1}{2}\rho \boldsymbol{V}_{\text{wing}}^2 S C_D(\alpha) \end{aligned} \tag{4.21}$$

Where $\boldsymbol{V}_{\text{wing}}$ is the flow at the wing, S is the UAV wing's planform. C_L and C_D are nondimensional aerodynamic coefficients. These coefficients can be found experimentally with wind tunnel testing, or theoretically. For small angles of α, approximately $|\alpha| = 10°$, the lift-coefficient can be modeled as $C_L(\alpha) \approx C_{L_0}\alpha$. The drag-coefficient can be approximated with $C_D(\alpha) \approx C_{D_0}$.

The lift and drag forces can be decomposed into the coordinate system of the wing by formula according to figure 4.3

$$\begin{aligned} f_{i^{\text{wing}}} &= F_{\text{lift}} \sin(\alpha_{\text{wing}}) - F_{\text{drag}} \cos(\alpha_{\text{wing}}) \\ f_{k^{\text{wing}}} &= -F_{\text{lift}} \cos(\alpha_{\text{wing}}) - F_{\text{drag}} \sin(\alpha_{\text{wing}}) \\ \tau_{\text{wing}} &= 0 \end{aligned} \tag{4.22}$$

By applying the approximation $\alpha \approx \sin(2\alpha)/2 \approx \cos(\alpha)\sin(\alpha)$ and inserting equation 4.21, the formula 4.22 can be expressed as:

$$\begin{aligned} f_{i^{\text{wing}}} &= \frac{1}{2}\rho S(w_{\text{wing}}^2 C_{L_0} - u_{\text{wing}}||\boldsymbol{V}_{\text{wing}}||C_{D_0}) \\ f_{k^{\text{wing}}} &= -\frac{1}{2}\rho S(w_{\text{wing}}||\boldsymbol{V}_{\text{wing}}||C_{D_0} + w_{\text{wing}}u_{\text{wing}}C_{L_0}) \\ \tau_{\text{wing}} &= 0 \end{aligned} \tag{4.23}$$

This formula can be arranged on matrix form by defining a vector for the generalized force and velocity at the wing by

$$\boldsymbol{\lambda}_{\text{wing}} = \begin{bmatrix} f_{i^{\text{wing}}} \\ f_{k^{\text{wing}}} \\ \tau_{\text{wing}} \end{bmatrix} \qquad \boldsymbol{V}_{\text{wing}} = \begin{bmatrix} u_{\text{wing}} \\ w_{\text{wing}} \\ \omega_{\text{wing}} \end{bmatrix}$$

Leading to

$$\boldsymbol{\lambda}_{\text{wing}} = \frac{1}{2}\rho S \underbrace{\begin{bmatrix} -||\boldsymbol{V}_{\text{wing}}||C_{D_0} & w_{\text{wing}}C_{L_0} & 0 \\ -w_{\text{wing}}C_{L_0} & -||\boldsymbol{V}_{\text{wing}}||C_{D_0} & 0 \\ 0 & 0 & 0 \end{bmatrix}}_{\boldsymbol{A}(\boldsymbol{V}_{\text{wing}})} \cdot \boldsymbol{V}_{\text{wing}} \tag{4.24}$$

Now it is necessary to express the generalized force $\boldsymbol{\lambda}_{\text{wing}}$ in the body frame, $\mathcal{F}^b$. Figure 4.4 illustrates two wings placed at location $\mathbf{P}_1$ and $\mathbf{P}_2$, respectively. Furthermore, they are tilted

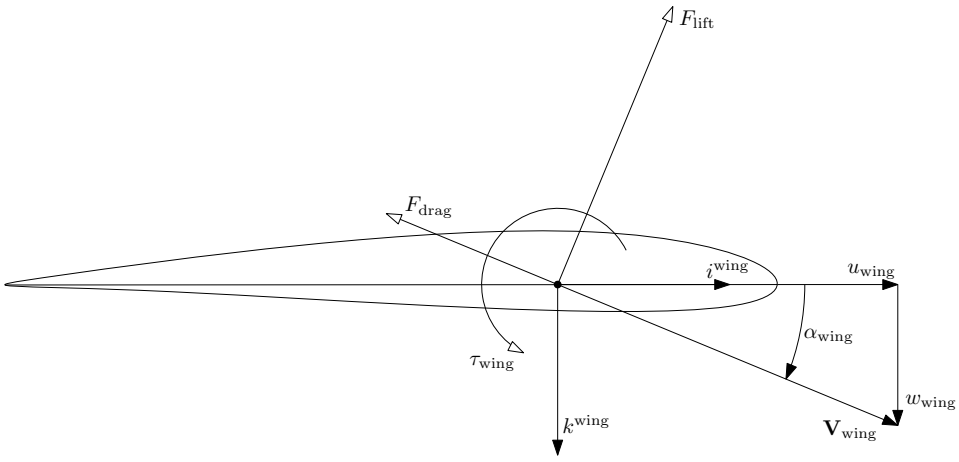

Figure 4.3: Illustration of the lift and drag force applied to an airfoil

by an angle of ι_*. The forces and moment at the body of the main wing (MW) is given according to

$$\begin{aligned} f_{i^{\text{body}}} &= f_{i^{\text{wing}}} \cos(\iota_1) - f_{k^{\text{wing}}} \sin(\iota_1) \\ f_{k^{\text{body}}} &= f_{i^{\text{wing}}} \sin(\iota_1) + f_{k^{\text{wing}}} \cos(\iota_1) \\ \tau_{\text{body}} &= -f_{i^{\text{body}}} p_2 + f_{k^{\text{body}}} p_1 + \tau_{\text{wing}} \end{aligned} \tag{4.25}$$

where p_1 and p_2 are decomposed components of $\mathbf{P}_1$. On matrix form the equation 4.25 becomes

$$\boldsymbol{\lambda}_{\text{body}} = \underbrace{\begin{bmatrix} \cos(\iota_1) & \sin(\iota_1) & 0 \\ -\sin(\iota_1) & \cos(\iota_1) & 0 \\ -p_2\cos(\iota_1) - p_1\sin(\iota_1) & -p_2\sin(\iota_1) + p_1\cos(\iota_1) & 1 \end{bmatrix}}_{\boldsymbol{K}} \cdot \boldsymbol{\lambda}_{\text{wing}} \tag{4.26}$$

where $\boldsymbol{K}$ can be simplified into

$$\boldsymbol{K} = \underbrace{\begin{bmatrix} 1 & 0 & 0 \\ 0 & 1 & 0 \\ -p_2 & p_1 & 1 \end{bmatrix}}_{\boldsymbol{L}} \cdot \underbrace{\begin{bmatrix} \cos(\iota_1) & \sin(\iota_1) & 0 \\ -\sin(\iota_1) & \cos(\iota_1) & 0 \\ 0 & 0 & 1 \end{bmatrix}}_{\boldsymbol{P}} \tag{4.27}$$

The power is defined as the product of velocity and force, hence $P = \boldsymbol{V}_{\text{wing}}^{\top} \boldsymbol{\lambda}_{\text{wing}}$ or $P = \boldsymbol{V}_{\text{body}}^{\top} \boldsymbol{\lambda}_{\text{body}}$. Then an equation that relates body velocities to the wing velocities can be derived:

$$\begin{aligned} P = \boldsymbol{V}_{\text{wing}}^{\top} \boldsymbol{\lambda}_{\text{wing}} = \boldsymbol{V}_{\text{wing}}^{\top} \boldsymbol{K} \boldsymbol{\lambda}_{\text{body}} = (\boldsymbol{K}^{\top} \boldsymbol{V}_{\text{body}})^{\top} \boldsymbol{\lambda}_{\text{body}} \\ \Rightarrow \boldsymbol{V}_{\text{wing}} = \boldsymbol{K}^{\top} \boldsymbol{V}_{\text{body}} \end{aligned} \tag{4.28}$$

In the absence of wind, $\boldsymbol{V}_{\text{body}}$ is equal to the state variable $\boldsymbol{\nu}$ with the longitudinal terms. The point force in the wing frame is mapped to a generalized force in the body frame

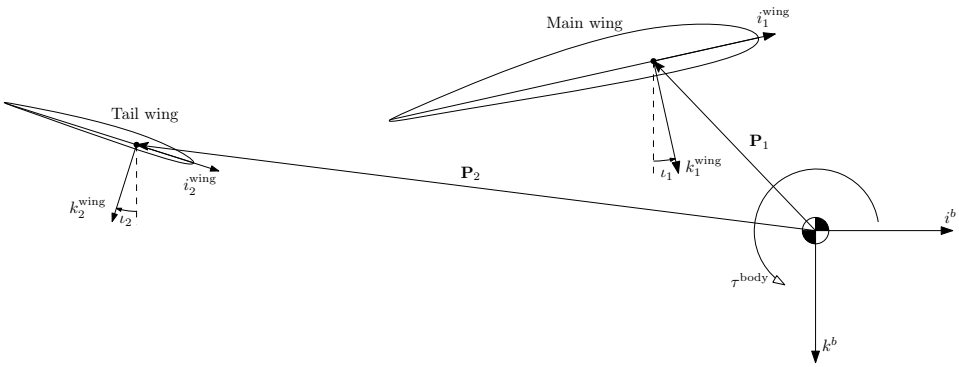

Figure 4.4: Illustration of forces defined by the wing frame in relation to to the body frame

through the transformation:

$$\boldsymbol{\tau}_{MW} = \boldsymbol{K}\boldsymbol{\lambda}_{\text{wing}} \tag{4.29}$$

Inserting the aerodynamic model into this relation yields

$$\boldsymbol{\tau}_{MW} = \boldsymbol{K}\boldsymbol{A}(\boldsymbol{V}_{\text{wing}})\boldsymbol{V}_{\text{wing}} \tag{4.30}$$

Finally, by inserting equation 4.28 and assume zero wind. The forces and moments propagated from the main wing acting at the body frame is given by

$$\boldsymbol{\tau}_{MW} = \underbrace{\boldsymbol{K}\boldsymbol{A}(\boldsymbol{K}^\top\boldsymbol{\nu})\boldsymbol{K}^\top}_{\boldsymbol{B}_{MW}} \cdot \boldsymbol{\nu} \tag{4.31}$$

Now it is possible to integrate a tail wing (TM) at the rear of the UAV, derived with the same procedure as the main wing. The final force acting at the center of gravity due to wing forces and moments given in the body frame is written as

$$\boldsymbol{\tau}_{\text{aero}}^{\text{long}} = (\boldsymbol{B}_{MW} + \boldsymbol{B}_{TM})\boldsymbol{\nu} \tag{4.32}$$

Moving mass modelling

In level flight, $\theta = 0$, a forward moved mass will generate a nose down moment according to $\tau_m = -m_{\text{long}} g \delta_m$. The net generalized force on the UAV can be written as

$$\boldsymbol{\tau}_{\text{mass}}^{\text{long}} = g\, m_{\text{long}} \begin{bmatrix} 0 \\ 0 \\ -\cos(\theta) \end{bmatrix} \delta_m \tag{4.33}$$

A moving mass affects the inertia tensor matrix of an aircraft. The kinetic energy for the system follows

$$T = \frac{1}{2}\boldsymbol{\nu}^\top \boldsymbol{M}_{RB}\boldsymbol{\nu} \tag{4.34}$$

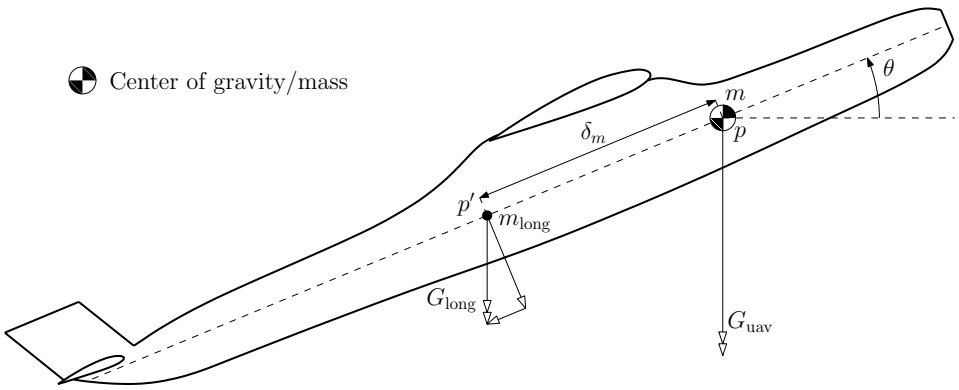

Figure 4.5: Moving mass illustration longitudinally

It is assumed that this expression includes the moving mass element m_{long} when located at position p. When the mass moves to a new position p', the energy stored at p is removed, and new energy adds to location p'. The absolute plane velocity squared $U^2(p)$ at any point in the body frame may be written as

$$U^2(p) = (\mathbf{\Pi} \boldsymbol{L}^\top(p)\boldsymbol{\nu})^\top (\mathbf{\Pi} \boldsymbol{L}^\top(p)\boldsymbol{\nu}) \tag{4.35}$$

where $\boldsymbol{L}$ is the matrix form equation 4.27 with p_2 equal to zero due to mass is only moving in one direction in body frame $\mathcal{F}^b$. $\mathbf{\Pi}$ is added for removing the rotational component, which is irrelevant for the energy of a point mass, thus;

$$\mathbf{\Pi} = \begin{bmatrix} 1 & 0 & 0 \\ 0 & 1 & 0 \\ 0 & 0 & 0 \end{bmatrix}$$

The energy difference for adding mass at location p' and subtracting at p yields

$$\begin{aligned} \frac{m_{\text{long}}}{2}(U^2(p') - U^2(p)) &= \frac{m_{\text{long}}}{2}(\mathbf{\Pi} \boldsymbol{L}^\top(p')\boldsymbol{\nu})^\top (\mathbf{\Pi} \boldsymbol{L}^\top(p')\boldsymbol{\nu}) \\ &- \frac{m_{\text{long}}}{2}(\mathbf{\Pi} \boldsymbol{L}^\top(p)\boldsymbol{\nu})^\top (\mathbf{\Pi} \boldsymbol{L}^\top(p)\boldsymbol{\nu}) \\ &= \frac{m_{\text{long}}}{2}\boldsymbol{\nu}^\top (\boldsymbol{L}(p')\mathbf{\Pi} \boldsymbol{L}^\top(p') - \boldsymbol{L}(p)\mathbf{\Pi} \boldsymbol{L}^\top(p))\boldsymbol{\nu} \\ &= \frac{m_{\text{long}}}{2}\boldsymbol{\nu}^\top \begin{bmatrix} 0 & 0 & 0 \\ 0 & 0 & -\Delta P \\ 0 & -\Delta P & p'^2 - p^2 \end{bmatrix} \boldsymbol{\nu} \end{aligned} \tag{4.36}$$

where $\Delta P = p' - p$, now let

$$\Delta \boldsymbol{M}_{RB} = \frac{m_{\text{long}}}{2} \begin{bmatrix} 0 & 0 & 0 \\ 0 & 0 & -\Delta P \\ 0 & -\Delta P & p'^2 - p^2 \end{bmatrix} \tag{4.37}$$

The rigid-body mass matrix changes as $\boldsymbol{M}_{RB} \rightarrow \boldsymbol{M}_{RB} + \Delta\boldsymbol{M}_{RB}$ when the mass moves from p to p'. However, a reasonable assumption is that ΔP is small enough, and the mass matrix does not change appreciably. Furthermore, the rigid-body mass matrix enters the dynamics as a multiplier for quantities that ought to be small, i.e., accelerations and the pitch rate. Therefore it is reasonable to assume $\Delta\boldsymbol{M}_{RB}$ equal zero.

Propulsion force

A simple model for the propulsion forces generated by a propeller is presented by Beard and McLain (2012)[4] and is repeated here for ease of reference. Calculating the pressure difference ahead and behind of the propeller with the principle of Bernoulli will result in a model that is correct for a perfectly efficient propeller. However, the model is highly optimistic in its thrust predictions, [4]. The total pressure upstream and downstream is given by:

$$P_{\text{upstream}} = P_0 + \frac{1}{2}\rho V_a^2 \tag{4.38a}$$

$$P_{\text{downstream}} = P_0 + \frac{1}{2}\rho V_{\text{exit}}^2 \tag{4.38b}$$

where P_0 is the static pressure and V_{exit} is the speed of the air that leaves the propeller, and denoted:

$$V_{\text{exit}} = k_{\text{motor}}\delta_t$$

δ_t is the puls-width-modulation (PWM) input and k_{motor} is a motor constant. The thrust generated by the motor is then given by:

$$\begin{aligned} F_x &= S_{\text{prop}}C_{\text{prop}}(P_{\text{downstream}} - P_{\text{upstream}}) \\ &= \frac{1}{2}\rho S_{\text{prop}}C_{\text{prop}}\left[(k_{\text{motor}}\delta_t)^2 - V_a^2\right] \end{aligned}$$

Finally, can the propulsion force acting in the body frame can be expressed as:

$$\tau_{\text{prop}}^{\text{long}} = \frac{1}{2}\rho S_{\text{prop}}C_{\text{prop}} \begin{bmatrix} (k_{\text{motor}}\delta_t)^2 - V_a^2 \\ 0 \\ 0 \end{bmatrix} \tag{4.39}$$

The thrust is assumed to act along the i^b body axis of the UAV, and therefore no moments about the center of gravity will be generated.

Summary of longitudinal equation of motion

The longitudinal terms are derived by assuming that the lateral states are zeros (i.e., $\phi = \psi = r = p = v = 0$ in equation 4.10 and 4.12. Windspeed is also assumed to be zero also. The longitudinal equation of motion can be summarized in the matrix form as:

$$\dot{\boldsymbol{\eta}}^{\text{long}} = \boldsymbol{J}_{\boldsymbol{\Theta}}{}^{\text{long}} \cdot \boldsymbol{\nu}^{\text{long}} \tag{4.40a}$$

$$\boldsymbol{M}_{RB}^{\text{long}}\dot{\boldsymbol{\nu}}^{\text{long}} + \boldsymbol{C}_{RB}^{\text{long}}\boldsymbol{\nu}^{\text{long}} = \boldsymbol{\tau}_{RB}^{\text{long}} + \boldsymbol{g}^{\text{long}} \tag{4.40b}$$

where $\boldsymbol{\nu}^{\text{long}} = [u, w, q]^\top$, $\boldsymbol{\eta}^{\text{long}} = [x^n, h, \theta]^\top$ and $\boldsymbol{\tau}_{RB}^{\text{long}} = \boldsymbol{\tau}_{\text{aero}}^{\text{long}} + \boldsymbol{\tau}_{\text{prop}}^{\text{long}} + \boldsymbol{\tau}_{\text{mass}}^{\text{long}}$.

$$\boldsymbol{J_\Theta}^{\text{long}} = \begin{bmatrix} \cos(\theta) & \sin(\theta) & 0 \\ -\sin(\theta) & \cos(\theta) & 0 \\ 0 & 0 & 1 \end{bmatrix}$$

$$\boldsymbol{M}_{RB}^{\text{long}} = \begin{bmatrix} m & 0 & 0 \\ 0 & m & 0 \\ 0 & 0 & I_{yy} \end{bmatrix}, \quad \boldsymbol{C}_{RB}^{\text{long}} = \begin{bmatrix} 0 & q & 0 \\ -q & 0 & 0 \\ 0 & 0 & 0 \end{bmatrix}, \quad \boldsymbol{g}^{\text{long}} = \begin{bmatrix} -mg\,\sin(\theta) \\ mg\,\cos(\theta) \\ 0 \end{bmatrix}$$

Chapter 5

Methods and Procedure

A CAD of a UAV with moving mass actuation is first presented with design considerations. Furthermore, the airfoil choice and software framework are described in more detail. The derived non-linear equation of motion in chapter 4 are then linearized around trim points, and state-space representation of the UAV is introduced. After that, the actuator dynamics of the moving mass and integral term for the LQR controller are augmented to the state-space model. Finally, the different controllers with tuning parameters are presented.

5.1 UAV and Moving Mass Actuation Design

A UAV with moving mass actuation is designed in SolidWorks shown in figure 5.1. This study focuses only on longitudinal moving mass control (MMC), but the UAV is designed with the possibility of integrating lateral MMC. The lateral and longitudinal moving mass must operate independently without intersecting. Therefore, the main wing and fuselage cannot lay at the same level unless the UAV is equipped with two lateral MMC located in each wing. Reference is made to the study by Wang et al. [16]. The only practical moving mass for a UAV with an electrical propulsion system is the batteries. With this solution, no additional mass is added.

Weight, available space, power consumption, and assembly are some design considerations for the MMC. Vengate [19] used two linear actuators placed in the main wing to create a lateral moment, see figure 2.3. A linear actuator limits the available displacement for a moving mass compared to a mass moving along a rail connected to a motor. This concept will be explored further, because a lighter mass can be used with a longer travel length creating the necessary moment. Accurate and precise movement is essential for sufficient control of the UAV with MMC. Hence, a stepper motor is preferred over a brushless dc motor. Stepper motors are found in 3D printers, robot arms, and CNC milling machines, where precise position control is required. Also, a stepper motor is an excellent choice where a load needs to be held in place due to holding torque. Nevertheless, the power consumption is independent of the load, meaning a constant maximum current is drawn.

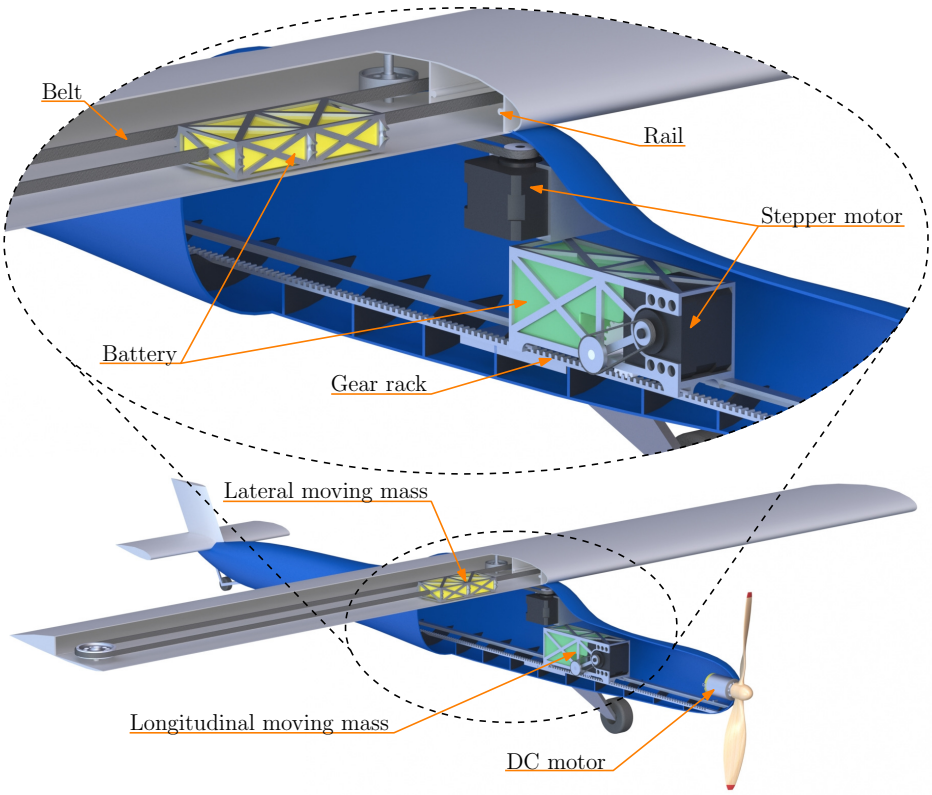

Figure 5.1: Render of UAV with moving mass

Two hybrid permanent magnet stepper motors from RC Components are chosen for the MMC system, one longitudinally and one lateral. The weight of the motor is 220 g.

Erturk (2016)[17] used a longitudinal moving mass weighing approximately 16% of the UAV's total weight. Therefore the stepper motor is included in the longitudinally MMC system to gain sufficient load. Figure 5.1 shows the longitudinally MMC system with an option for two-step downshifting to achieve desired speed and torque. The MMC is assumed to move frictionless on two rails with a gear rack in the middle to transform rotational motion from the motor to longitudinal motion. There is limited space for a moving mass in the main wing, and the stepper motor is not included. Also, Erturk (2016)[17] applied a lower weight for the lateral MMC, about 5% of the UAV's total weight. The UAV is designed with an aspect ratio (ratio between wingspan and mean chord) of seven. An aspect ratio lower than five results in an airplane with more agile but less stable characteristics. The Cessna 172 has an aspect ratio of 7.32 and is equipped with the NACA-2412 airfoil, [32]. This is a semi-symmetrical airfoil, meaning no initial angle of attack is required

Table 5.1: Parameters for UAV

Parameters	Value	Description
m	$3.5\,kg$	Weight of UAV
m_{long}	$0.4\,kg$	Weight of longitudinal moving mass
I_{yy}	$0.148\,kg\,m^2$	Element of inertia matrix in the x-z plane
S_{prop}	$0.0314\,m^2$	Aera of the propeller
C_{prop}	1	Aerodynamic coefficient for the propeller
k_{motor}	25	Constant that specifies the efficiency of the motor
S_{MW}	$0.28\,m^2$	Surface area of the main wing
b_{MW}	$1.4\,m$	Wing span of main wing
AR_{MW}	7	Aspect ratio of main wing
S_{TW}	$0.02\,m^2$	Surface area of the tail wing
b_{TW}	$0.25\,m$	Wing span of tail wing
AR_{TW}	3.13	Aspect ratio of tail wing
C_{D_0}	0.026	Aerodynamic drag coefficient
C_{L_0}	0.308	Aerodynamic lift coefficient
L_1	$0.1\,m$	Horizontal distance from CG to aerodynamic center of main wing
H_1	$0.08\,m$	Vertical distance from CG to aerodynamic center of main wing
ι_1	0°	Rotation of main wing
L_2	$0.76\,m$	Horizontal distance from CG to aerodynamic center of tail wing
H_2	$0.01\,m$	Vertical distance from CG to aerodynamic center of tail wing
ι_2	4°	Rotation of tail wing
p_f	$0.2\,m$	Movable space forward in UAV
p_b	$0.455\,m$	Movable space backward in UAV

to take off compared to a symmetrical airfoil. However, The NACA-2412 has an airfoil thickness of 12% of the chord length and can be problematic for the available space for a lateral MMC. Therefore, NACA-2414 was chosen, which is 14% of the chord length and has a semi-symmetrical airfoil. The lift and drag coefficient for the airfoil is obtained from the study by Kulshreshtha et al. [33].

The main and tail wing position on the fuselage is essential for aircraft stability dynamics as described in chapter 3.1, and after iterative simulation workflow, the best location of the tail wing was 760 mm behind and 10 mm above the center of gravity (CG). At the same time, the main wing was positioned 100 mm behind and 80 mm above CG. The main and tail wing is angled 0 and 4 degrees, respectively. See figure 4.4 for the positive direction of the tilt angle. All the parameter for the UAV is summarized in table 5.1. For longitudinal motion, only I_{yy} is of interest and is assumed to be constant. The I_{yy} is determined with the moving mass CG coincident with the UAV's CG.

5.2 Software

The software framework used in the simulation is Simulink and MATLAB. For the successive loop closure method, the PID controllers are tuned with the auto-tuned capabilities

in Simulink. There are two different tuning tools: Transfer Function Based (TFB) and Frequency Response Based (FRB). The main difference between these tuning tools is that FRB is more suitable for plants that are not linearizable or linearized to zero. Nevertheless, the plant is linearizable, and TFB is chosen. TFB enables the user to examine the system response while interactively tuning PID coefficients,[34]. The optimal control gains $\mathbf{K}$ for the LQR controller is calculated using *lqr* command in MATLAB.

Simulink provides a tool library named Aerospace Blockset for modeling, simulating, and analyzing aircraft and spacecraft platforms. The Incidence & Airspeed block from this toolbox are used for calculating absolute velocity and angle of attack from the components of the velocity vector(u,w) in the body.

5.3 Linearization and State-Space Model

The equation of motion from chapter 4 is linearized in this section for analyzing controllability and stability. Furthermore, state-space representation eases the design of controllers in Simulink and MATLAB. The equation 4.40b can be rewritten as

$$\dot{\boldsymbol{\nu}}^{long} = \boldsymbol{M}_{RB}^{-1} \cdot \left(-\boldsymbol{C}_{RB}^{long} \boldsymbol{\nu}^{long} + \boldsymbol{\tau}_{RB}^{long} + \boldsymbol{g}^{long} \right) \tag{5.1}$$

Now the kinematics and dynamics are represented in a compact form as

$$\mathbf{f} = \begin{bmatrix} \dot{\boldsymbol{\nu}}^{long} \\ \dot{\boldsymbol{\eta}}^{long} \end{bmatrix} \tag{5.2}$$

The state space model on form $\dot{\mathbf{x}} = \mathbf{A}\mathbf{x} + \mathbf{B}\mathbf{u}$ is derived by

$$\boldsymbol{A} = \left. \frac{\partial \mathbf{f}}{\partial \mathbf{x}} \right|_{\mathbf{x_0},\, \mathbf{u_0}} = \begin{bmatrix} \frac{\partial \dot{u}}{\partial u} & \frac{\partial \dot{u}}{\partial w} & \frac{\partial \dot{u}}{\partial q} & \frac{\partial \dot{u}}{\partial h} & \frac{\partial \dot{u}}{\partial \theta} \\ \frac{\partial \dot{w}}{\partial u} & \frac{\partial \dot{w}}{\partial w} & \frac{\partial \dot{w}}{\partial q} & \frac{\partial \dot{w}}{\partial h} & \frac{\partial \dot{w}}{\partial \theta} \\ \frac{\partial \dot{q}}{\partial u} & \frac{\partial \dot{q}}{\partial w} & \frac{\partial \dot{q}}{\partial q} & \frac{\partial \dot{q}}{\partial h} & \frac{\partial \dot{q}}{\partial \theta} \\ \frac{\partial \dot{h}}{\partial u} & \frac{\partial \dot{h}}{\partial w} & \frac{\partial \dot{h}}{\partial q} & \frac{\partial \dot{h}}{\partial h} & \frac{\partial \dot{h}}{\partial \theta} \\ \frac{\partial \dot{\theta}}{\partial u} & \frac{\partial \dot{\theta}}{\partial w} & \frac{\partial \dot{\theta}}{\partial q} & \frac{\partial \dot{\theta}}{\partial h} & \frac{\partial \dot{\theta}}{\partial \theta} \end{bmatrix}_{\mathbf{x_0},\, \mathbf{u_0}} \tag{5.3a}$$

$$\boldsymbol{B} = \left. \frac{\partial \mathbf{f}}{\partial \mathbf{u}} \right|_{\mathbf{x_0},\, \mathbf{u_0}} = \begin{bmatrix} \frac{\partial \dot{u}}{\partial \delta_m} & \frac{\partial \dot{u}}{\partial \delta_t} \\ \frac{\partial \dot{w}}{\partial \delta_m} & \frac{\partial \dot{w}}{\partial \delta_t} \\ \frac{\partial \dot{q}}{\partial \delta_m} & \frac{\partial \dot{q}}{\partial \delta_t} \\ \frac{\partial \dot{h}}{\partial \delta_m} & \frac{\partial \dot{h}}{\partial \delta_t} \\ \frac{\partial \dot{\theta}}{\partial \delta_m} & \frac{\partial \dot{\theta}}{\partial \delta_t} \end{bmatrix}_{\mathbf{x_0},\, \mathbf{u_0}} \tag{5.3b}$$

where $\mathbf{x_0} = [u_0, w_0, q_0, h_0, \theta_0]^\top$ and $\mathbf{u_0} = [\delta_{m_0}, \delta_{t_0}]^\top$ are trim values.

It is assumed that the UAV is equipped with an Inertia Measurement Unit (IMU), pressure and airspeed sensor, and a global positioning system (GPS), so that all states can be measured. I.e. C matrix of the equation $\mathbf{y} = \mathbf{Cx} + \mathbf{Du}$ is equal to the identity matrix. Furthermore, the measured states are not affected by the inputs, i.e. D matrix is zero.

The nonlinear equations of forces acting on the UAV, ref 4.20 were examined with simple trimming analysis involving Newton's method to find a balance point where the gravity and aerodynamic lift force are in equilibrium. However, finding trim condition is not a trivial task, and after iterations and simulation of the open-loop response, the following trim values were chosen:

$$\mathbf{x_0} = \begin{bmatrix} u_0 \\ w_0 \\ q_0 \\ h_0 \\ \theta_0 \end{bmatrix} = \begin{bmatrix} 9.9985 \\ 0.1745 \\ 0 \\ 0 \\ 0 \end{bmatrix} \qquad \mathbf{u_0} = \begin{bmatrix} \delta_{m_0} \\ \delta_{t_0} \end{bmatrix} = \begin{bmatrix} 0 \\ 0.5 \end{bmatrix} \tag{5.4}$$

This is equivalent to an airspeed of 10 m/s with an angle of attack equal to 1 degree. The MATLAB script for calculating the equation of motion in chapter 4 and defining the linearized state-space representation is enclosed in appendix A. The linearization is based on the assumption that pitch angle and angle of attack are small, namely $|\theta| < 15^\circ$ and $|\alpha| < 10^\circ$. The longitudinal state-space model of the UAV becomes:

$$\begin{aligned} \boldsymbol{A} &= \begin{bmatrix} -0.1421 & 0.0028 & -0.0475 & 0 & -9.8100 \\ -0.0016 & -0.1814 & 2.8308 & 0 & 0 \\ 0.0676 & -0.6271 & -0.2095 & 0 & 0 \\ 0 & -1.0000 & 0 & 0 & 9.9985 \\ 0 & 0 & 1.0000 & 0 & 0 \end{bmatrix} \\ \boldsymbol{B} &= \begin{bmatrix} 0 & 3.5555 \\ 0 & 0 \\ -26.5135 & 0 \\ 0 & 0 \\ 0 & 0 \end{bmatrix} \end{aligned} \tag{5.5}$$

5.4 Introducing Delay in Moving Mass Actuation

The moving mass actuation is augmented to the longitudinal equation of motion given in 5.5 as state δ_t, and is modeled as a low-pass filter (H_m(s)) with time constant $T_m = \frac{1}{N} = 1/10$s. The transfer function is given by:

$$H_m(s) = \frac{\delta_m}{\delta_m^c} = \frac{N}{s+N} = \frac{1}{\frac{1}{N}+1} = \frac{1}{T_m s + 1} = \frac{10}{s+10} \tag{5.6}$$

where δ_m^c is the control input and δ_m is the actual state. The final state space representation becomes

$$\boldsymbol{A}_{\text{SLC}} = \begin{bmatrix} -0.1421 & 0.0028 & -0.0475 & 0 & -9.8100 & 0 \\ -0.0016 & -0.1814 & 2.8308 & 0 & 0 & 0 \\ 0.0676 & -0.6271 & -0.2095 & 0 & 0 & -26.5135 \\ 0 & -1.0000 & 0 & 0 & 9.9985 & 0 \\ 0 & 0 & 1.0000 & 0 & 0 & 0 \\ 0 & 0 & 0 & 0 & 0 & -10.0000 \end{bmatrix} \mathbf{x}$$
$$\boldsymbol{B}_{\text{SLC}} = \begin{bmatrix} 0 & 3.5555 \\ 0 & 0 \\ 0 & 0 \\ 0 & 0 \\ 0 & 0 \\ 10.0000 & 0 \end{bmatrix} \mathbf{u} \tag{5.7}$$

where $\mathbf{x} = [u, w, q, h, \theta, \delta_t]^\top$ and $\mathbf{u} = [\delta_m, \delta_t]^\top$

5.5 Successive Loop Closure

Two control designs are examined; optimal control with Linear Quadratic Regulator (LQR) and several PID controllers design. The PID controller design is shown in figure 5.2 with the state-space model from equation 5.7 in the orange block. The *Demux and conversion* subsystem calculates the absolute velocity from state u and w and rearranges the order of the states. The design consists of three PID controllers: one controls the airspeed, while the second controls the moving mass with input from the third controller, setting a pitch angle with respect to commanded altitude. The yellow block is a transfer function from pitch angle to altitude given by

$$h(s) = \frac{1}{s}\theta \cdot V_a \tag{5.8}$$

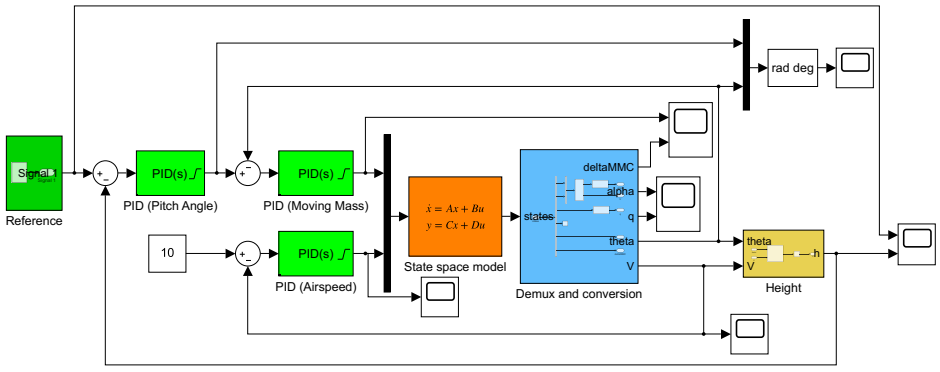

Figure 5.2: Successive loop closure controller design

This function gives a good approximation for constant airspeed since the pitch angle influences the climb rate. Simulations also showed that equation 5.8 gave a better approximation than the height state from the model. Now the complete ascend/descend and altitude hold is given by two models that can be closed individually. The PID controllers are tuned with the auto-tune capabilities in Simulink, with the request for the inner loop to act faster than the outer loop in mind. Table 5.2 shows an overview of coefficients and performance of the tuned PID controllers used for simulation. The impact on the system by changing the controller parameters is described in chapter 3.2. Both k_d is small and negative for the pitch angle and airspeed controller. A negative value reduces damping and makes the system act faster. However, k_d is small and can be disregarded, leading to only two PI regulators in practice.

The filter coefficient N is the same in equation 5.6 because it is common to implement a low-pass filter in series with the derivative term to remove noise from the signal, where N is rad/s and specifies which frequencies to dampen. Rise time defines the amount of time the plant uses from 10% to 90% of the reference. The pitch angle controller has about seven times longer settling time than the moving mass controller, ensuring the bandwidth request. Overshoot specifies in percent how much the system exceeds the reference. Peak is the same as overshoot and represents the highest value with which the system exceeds the reference value of 1. The gain and phase margin specifies the amount of gain or phase that can be increased/decreased without the system becoming unstable. The system can contain uncertainties concerning friction in bearings that reduce the gain margin. Moreover, the plant model might not reflect the actual system. Phase margin is essential if a delay is introduced in the system due to a slow computer.

Table 5.2: Parameters and performance of the PIDs controllers

Controller Parameters	**PID (Airspeed)**	**PID (Moving Mass)**	**PID (Pitch Angle)**
k_p	2.472	0.314	0.238
k_i	3.903	0.025	0.077
k_d	-0.091	0.868	-0.007
N (Filter coefficient)	8.071	1571.906	18.214
Performance and Robustness			
Rise time	0.18 sec	0.0824 sec	0.574 sec
Settling time	1.38 sec	0.996 sec	7.32 sec
Overshoot	13.4 $\%$	52.6 $\%$	8.28 $\%$
Peak	1.13	1.53	1.08
Gain margin	Inf dB @ NaN rad/s	35.2 dB @ 118 rad/s	12.1 dB @ 13.8 rad/s
Phase margin	69 deg @ 8.07 rad/s	26.7 deg @ 13.8 rad/s	74.2 deg @ 2.44 rad/s

5.6 Linear Quadratic Regulator (LQR) and Integral Terms

The optimal control design is a MIMO (Multi-Input Multi-output) controller with state-feedback and reference-feed-forward of the following form:

$$\mathbf{u} = \mathbf{Fr} - \mathbf{Kx} \tag{5.9}$$

where the state-feedback matrix $\mathbf{K}$ is calculated with the LQR method, as described in chapter 3.2. The reference vector is $\mathbf{r} = [u, q, h, \theta]^\top$ and $\mathbf{F}$ is a function of terms in matrix $\mathbf{K}$ given by:

$$\mathbf{F} = \begin{bmatrix} K_{11} & K_{13} & K_{14} & K_{15} \\ K_{21} & K_{23} & K_{24} & K_{25} \end{bmatrix} \tag{5.10}$$

Integral effect for the state height is included to remove steady state error and is given by:

$$\dot{\gamma} = h - h_r \tag{5.11}$$

where h is the actual state and h_r is the height reference. The final state-space representation with optimal control is:

$$\begin{aligned} \boldsymbol{A}_{\text{LQR}} &= \begin{bmatrix} -0.1421 & 0.0028 & -0.0475 & 0 & -9.8100 & 0 & 0 \\ -0.0016 & -0.1814 & 2.8308 & 0 & 0 & 0 & 0 \\ 0.0676 & -0.6271 & -0.2095 & 0 & 0 & -26.5135 & 0 \\ 0 & -1.0000 & 0 & 0 & 9.9985 & 0 & 0 \\ 0 & 0 & 1.0000 & 0 & 0 & 0 & 0 \\ 0 & 0 & 0 & 0 & 0 & -10.0000 & 0 \\ 0 & 0 & 0 & 1.0000 & 0 & 0 & 0 \end{bmatrix} \mathbf{x} \\ \boldsymbol{B}_{\text{LQR}} &= \begin{bmatrix} 0 & 3.5555 \\ 0 & 0 \\ 0 & 0 \\ 0 & 0 \\ 0 & 0 \\ 10.0000 & 0 \\ 0 & 0 \end{bmatrix} \mathbf{u} \end{aligned} \tag{5.12}$$

where the final extended state vector becomes $\mathbf{x} = [u, w, q, h, \theta, \delta_t, \gamma]^\top$. Figure 5.3 shows an overview of the control structure in Simulink. The saturation block limits the movable mass as specified in table 5.1 and the $\delta_t = [0 - 1]$. The *Add act. height and integral term* block perform the equation 5.11. A complete overview of the control systems are enclosed in appendix B.

5.6.1 Tuning of LQR

Initially, the weighting matrix $\mathbf{Q}$ and $\mathbf{R}$ was set equal to the identity matrix. This resulted in overall good performance, except for the pitch rate with an unwanted high value, 60° deg/sec. When weighting the state q more, height tracking performances were reduced, resulting in

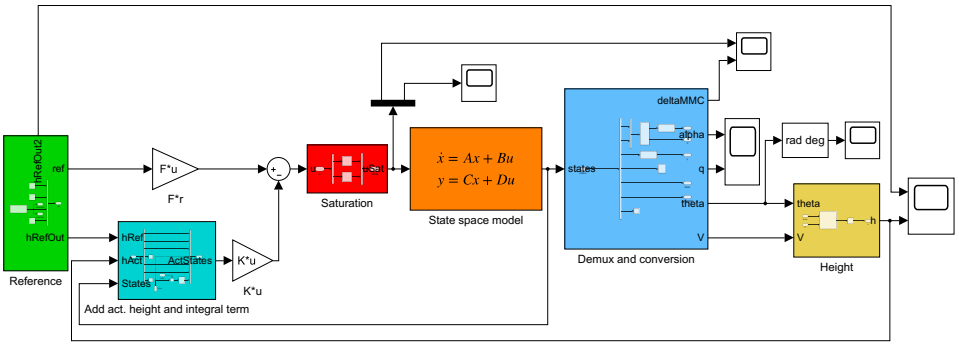

Figure 5.3: LQR Simulink

a slight overshoot between ascending/descending and altitude hold. Consequently, γ was weighted in order to reduce the steady-state error. Also, state u is vital for holding sufficient speed and preventing stall. In the effort to reduce the overshoot of height, the state h was weighted, but made the UAV more unstable at position (3) in figure 5.4. Minor adjustments were necessary for the $\mathbf{R}$ matrix and the final matrices became:

$$\mathbf{Q} = \begin{bmatrix} 30 & 0 & 0 & 0 & 0 & 0 & 0 \\ 0 & 1 & 0 & 0 & 0 & 0 & 0 \\ 0 & 0 & 120 & 0 & 0 & 0 & 0 \\ 0 & 0 & 0 & 1 & 0 & 0 & 0 \\ 0 & 0 & 0 & 0 & 20 & 0 & 0 \\ 0 & 0 & 0 & 0 & 0 & 1 & 0 \\ 0 & 0 & 0 & 0 & 0 & 0 & 5 \end{bmatrix} \qquad \mathbf{R} = \begin{bmatrix} 2 & 0 \\ 0 & 1 \end{bmatrix} \tag{5.13}$$

5.7 Height Reference

A reference generator is utilized for a smoother transition between the different altitude hold positions in figure 5.4 and ensuring stability in the system. The height reference for testing and analyzing the two different controllers is obtained by testing with different ascend and descend ratios to ensure the linearized model is valid. The controllers and the height reference are tuned interactively back and forth for an optimal basis of comparison. The resulting maximum ascends and descends ratios are 1.85 m/s and 2.00 m/s, respectively. This gives a pitch angle lover than $\pm 15^{\circ}$. The height reference consists of five altitude hold positions with a maximum ascend during take-off and up to 50 meters denoted (2). The simulation is conducted at a low altitude since the air density reduces with height and affects lift and drag coefficient, allowing air density to be assumed constant.

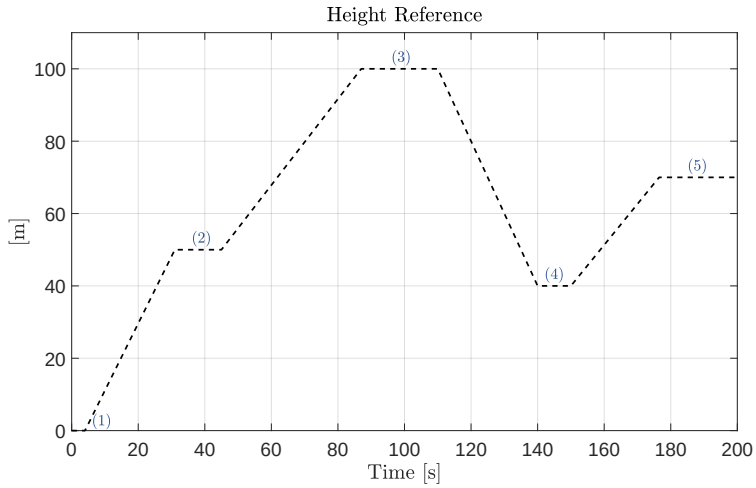

Figure 5.4: Height reference for analyzing and simulation

Chapter 6

Simulation and Results

This chapter presents the open-loop simulation comparing the flight behavior from the theory chapter. It also includes a comparison between the LQR and SLC controller. Then the different weight of the movable mass is tested and a simulation for obtaining maximum airspeed is performed. A simulation is conducted for a UAV with only throttle as input to demonstrate the importance of moving mass control. Finally, an analysis of the inertia tensor change is presented.

6.1 Open-Loop Simulation

The eigenvalues of the UAV can be computed by using the *damp.m* command in MATLAB on the matrix $\mathbf{A}$ from equation 5.7. The results are presented in table 6.1 with the eigenvalues plotted in figure 6.1. The phugoid and short-period mode terms from equation 3.3 becomes $\zeta_{\text{ph}} = 0.0071$, $\omega_{\text{ph}} = 1.34$, $\zeta_{\text{sp}} = 0.953$ and $\omega_{\text{sp}} = 0.27$. The damping ratio is reasonable where the phugoid mode is seen as a slow damped, oscillating behavior, whereas the short-period has more quickly well-damped characteristics. The eigenvalue -10 is from a moving mass actuation state and is perfectly damped. An interesting observation is that the imaginary part of the modes should have switched place to reflect the conventional aircraft pole placements from figure 3.3. The LQR controller with the state γ augmented to the state-space representation results in an additional pole at zero.

Table 6.1: Eigenvalues of UAV

Pole	Damping	Frequency [rad/s]	Time Constant [s]
0	-1	0	inf
-0.0095 + 1.3376i	0.0071	1.34	105
-0.0095 - 1.3376i	0.0071	1.34	105
-0.2571 + 0.0822i	0.953	0.27	3.89
-0.2571 - 0.0822i	0.953	0.27	3.89
-10	1	10	0.1

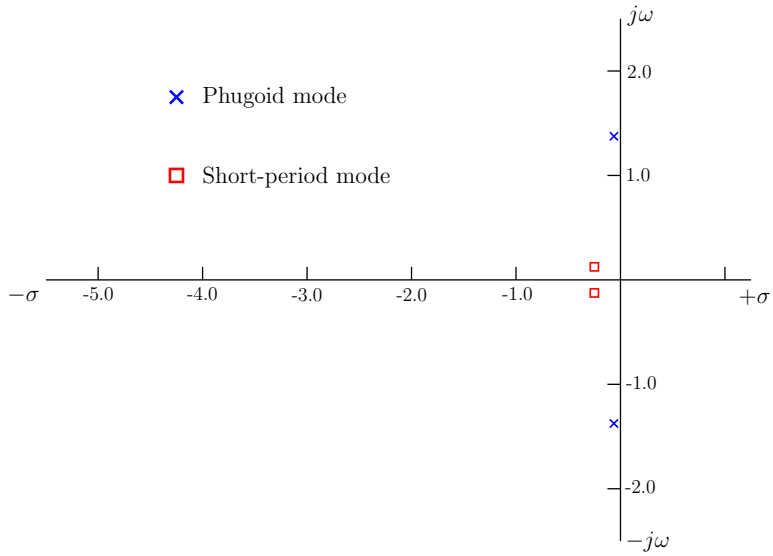

Figure 6.1: Eigenvalues for the UAV plotted in the s-plane

The open-loop dynamics are presented in figure 6.2 for the UAV with the moving mass at the fixed position of 0.0276 m. This position was where the moving mass was settling at a constant altitude and cruise speed of 10 m/s by utilizing the LQR controller. In figure 6.2a for the time interval 0 to 50 seconds, one can see the oscillation behavior caused by the phugoid mode. While the UAV increases speed, the lift force increase and tilt the UAV up. This process is repeated and ends with an almost constant descend ratio of 1.45 m/s. The simulation settles around a pitch angle of -8.3 degrees and oscillates with 2 degrees. The angle of attack settles with an oscillating behavior around -0.5 degrees with 0.5 degrees in amplitude. The absolute velocity ends at 10 m/s and with only 0.25 m/s in amplitude.

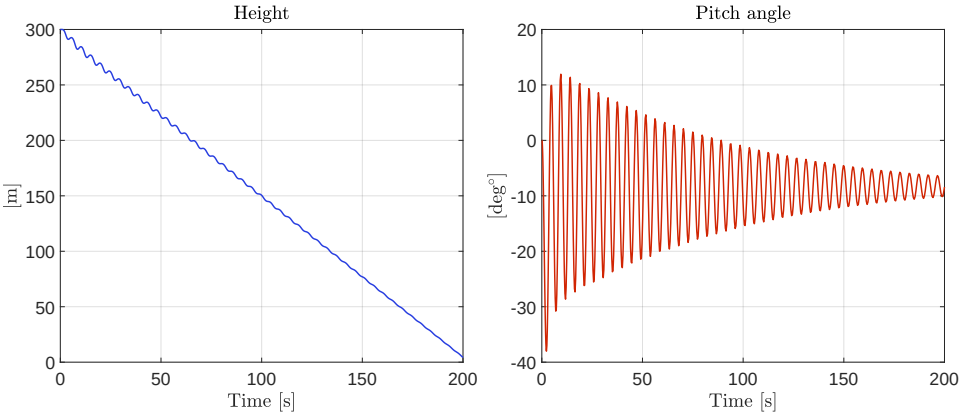

(a) Height

(b) Pitch Angle

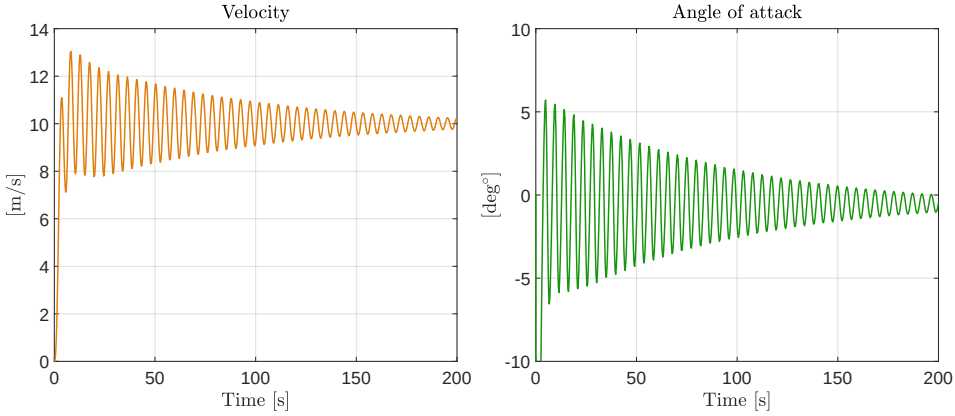

(c) Velocity

(d) Angle of Attack

Figure 6.2: Simulation of open-loop

6.2 Difference Between LQR and Successive Loop Closure

The different controllers track the height almost equally well, as seen in figure 6.3. Only the LQR controller has slightly more overshoot at the transition between ascending/descending to altitude hold. From figure 6.4a and 6.5b, the pitch angle and angle of attack is within the limits for the linearization limits $|\theta| < 15°$ and $|\alpha| < 10°$, respectively. An interesting observation is how the SLC controller requires a more travel length for the moving mass than LQR in figure 6.4b. This is a disadvantage since more travel increases the battery consummations and increases the pitch rate as seen in figure 6.5a. The total travel distance for the MMC is not fully utilized and the moving mass settles at position 0.0276 m from the origin. This entails that the UAV is not perfectly balanced with the moving mass at the pre-defined location from CAD. A slight constant deviation in the velocity for the

two controllers is seen in figure 6.5c. If the state u had been weighted more for the LQR controller, the difference would have been negligible. However, the LQR controller and the optimal **K** matrix is a compromise between states. If one state is weighted more, another will decline. Regarding the propulsion input in figure 6.5d, the LQR has a slightly higher dip than the SLC controller.

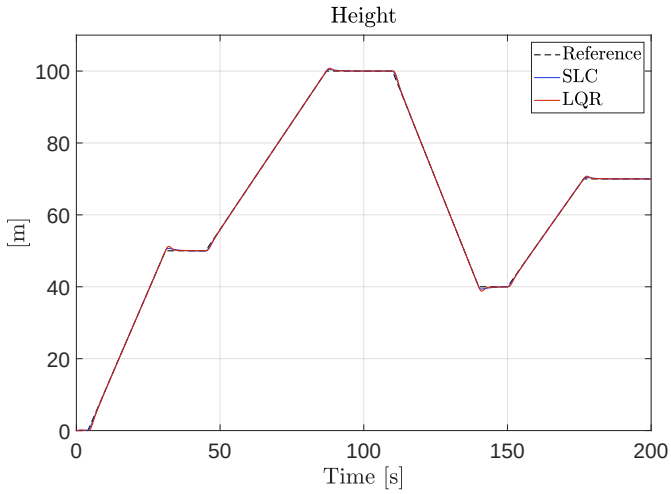

Figure 6.3: Comparison between LQR and successive loop closure (SLC)

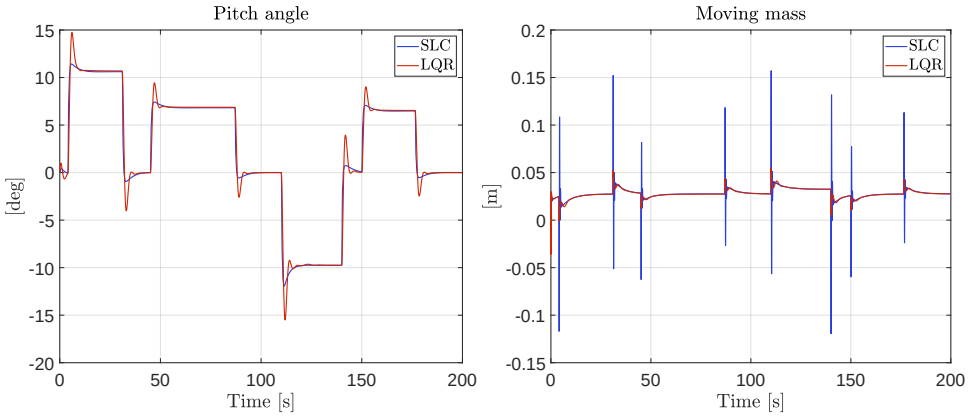

(a) Pitch angle

(b) Moving mass input

Figure 6.4: Pitch angle and moving mass position with different controllers

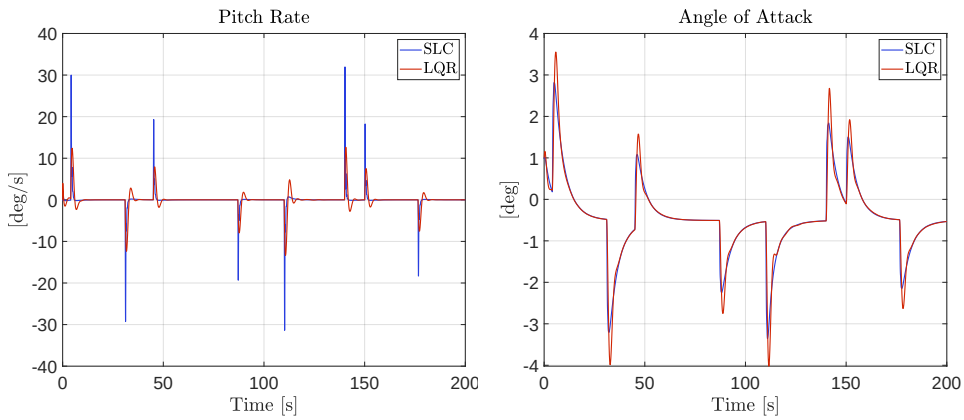

(a) Pitch rate

(b) Angle of attack

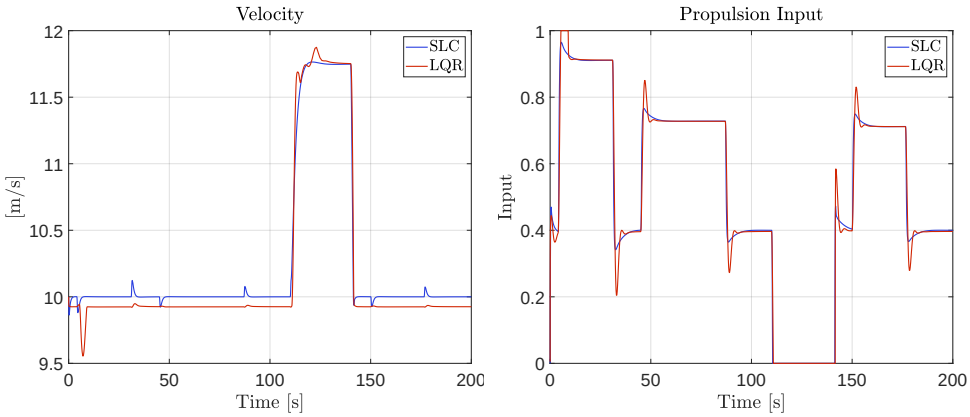

(c) Airspeed

(d) Propulsion input

Figure 6.5: Simulation of LQR versus successive loop closure (SLC) controller design

6.3 Different Weight of Moving Mass

Simulation with different weights on the longitudinal moving mass was conducted with the LQR controller. For a mass lighter than 50 grams, there was not enough moment to pitch the UAV down, as seen in figure 6.6. 60 grams was the lightest mass at which the UAV maintain control, but with poor tracking. Weight higher than 100 grams did not result in better tracking of the reference. However, increased mass gives improved descend capabilities. The CAD analysis gives a moving mass of 400 grams and this was chosen as the final weight.

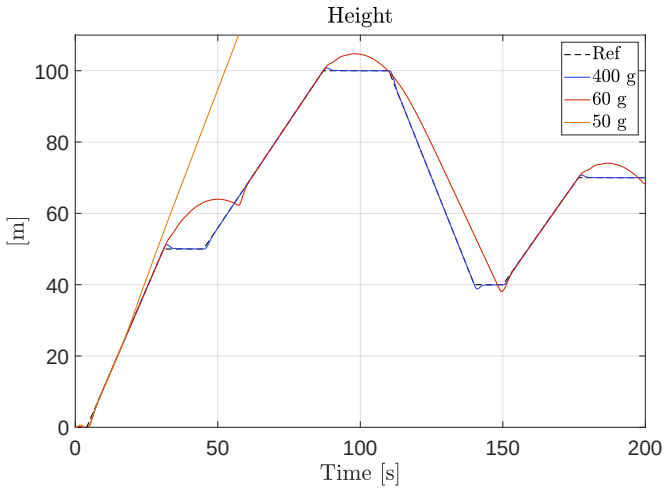

Figure 6.6: Different weight on moving mass with LQR control

6.4 Simulation of Constant Altitude While Increasing the Throttle Input Gradually

The purpose of this simulation is to illustrate the maximum velocity of the UAV with full throttle and how the moving mass moves forward with a maximum speed of 25 m/s, as seen in figure 6.7. The simulation also demonstrates that the UAV top speed is limited by the efficiency of the propulsion motor and not the weight of the moving mass. With less mass, the necessary moment for holding the UAV at straight level flight would not be sufficient and the UAV would start to ascend.

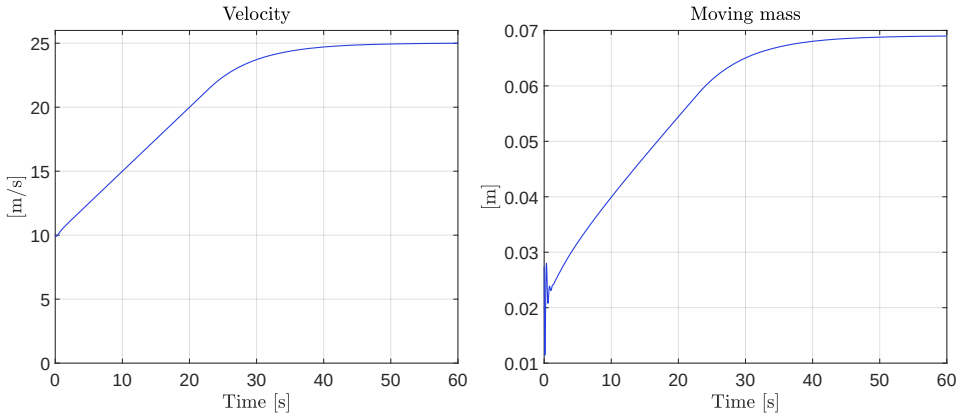

(a) Velocity

(b) Moving mass position

Figure 6.7: Straight level flight with increasing throttle

6.5 Only Throttle as Input

The moving mass is set to a fixed position at 0.0276 m, the same as for the open-loop simulation, only controlled with a PID controller on throttle input. In the effort of achieving satisfactory results, tuning the PID controller was a challenge. The controller is tuned with a slow response in order to stay stable. In the attempt to make the system faster, the k_p was increased, but this resulted in an unstable system. Table 6.2 summarizes the parameters for the PID controller. Since the integral term is small, the controller is in practice only a PD controller. Figure 6.8 shows the commanded and actual height with only propulsion input. The controller has a long settling time, and the consequence is that the UAV height is delayed over the whole reference specter. Clearly, at the start of the simulation, the UAV descends eight meters before the controller acts on the error and restores height. The UAV has problems with following the reference, especially for descending. Although the throttle input is set to zero, the highest descend rate is 1.45 m/s, showing the importance of moving mass control. Figure 6.9 presents the associated velocity and propulsion input.

Table 6.2: Parameters and performance of the PID with only propulsion

Controller Parameters	**PID**
k_p	0.0492
k_i	0.0009
k_d	-0.0328
N (Filter coefficient)	0.6346
Performance and Robustness	
Rise time	6.22 sec
Settling time	107 sec
Overshoot	18.2 $\%$
Peak	1.18
Gain margin	20 dB @ 0.969 rad/s
Phase margin	54.4 deg @ 0.176 rad/s

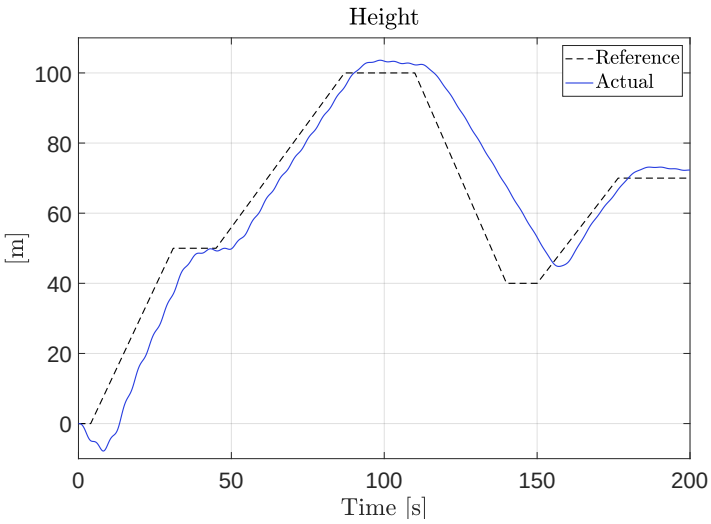

Figure 6.8: Height control with only propulsion

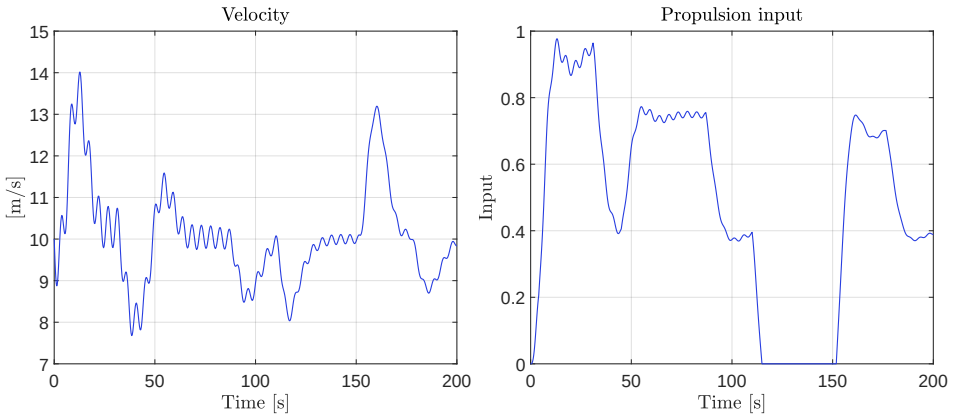

(a) Velocity

(b) Throttle input

Figure 6.9: Simulation with only controlling throttle

6.6 Moment of Inertia Tensor Analysis

The moment of inertia tensor, presented in equation 4.16, can be calculated in SolidWorks for a design at a fixed coordinate system. For symmetric bodies in the xz plane, only the changes in I_{xx}, I_{yy}, I_{zz} and $I_{xz} = I_{zx}$ are of interest. However, I_{xx} is constant only when the longitudinal moving mass is displaced. Figure 6.10 shows the I_{yy}, I_{zz} and I_{xz} at different positions of the moving mass. The zero-location spot is a fixed geometric point in the UAV and the same position as the center of mass in figure 3.1. The dashed lines in figure 6.10 is the polynominally fitted curves that conform to the parallel axis theorem

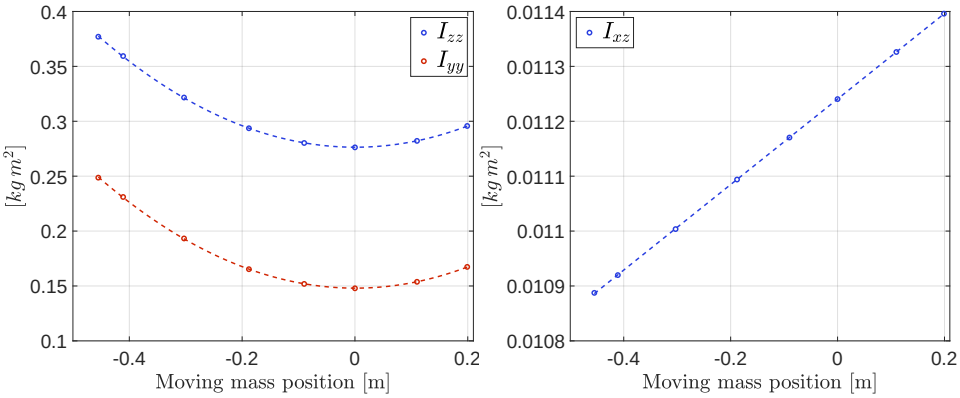

(a) Inertia terms I_{zz} and I_{yy}

(b) Inertia term I_{xz}

Figure 6.10: Changing of inertia tensor relative to the location of moving mass

for I_{yy} and I_{zz}. From the zero-point location and to the backward position, the I_{yy} and I_{zz} increases with 68% and 36%, respectively. Assuming the inertia is constant may be conservative for the equation of motion and should be taken into account. The I_{xz} follows a linear relationship, with only a total difference of 4.7% from backward to forward position.

Chapter 7

Discussion and Conclusion

The following section describes some topics that need to be discussed in addition to a conclusion. Finally, recommendations for future work are given.

This thesis is based on several assumptions. For instance, the angle of attack is assumed to be small and results in a linear function for the lift and drag coefficient of α. Additionally, the moving mass is modeled as an external force, like propulsion, without changing the system's dynamic response. It might be conservative applying linear theory on a complex system with coupled motion between the internal mass and the vehicle's body. Chapter 4 presents justification for these simplifications. A more comprehensive simulation must be established in order to gain more accurate results.

Whether the trim point in section 5.3 are the optimal trim values or not, can be discussed further. The result depends on the initial start values of Newton's method. The nonlinear function had several singularities, where the algorithm did not converge, and the UAV was not in equilibrium from the gravity/lift force and drag/propulsion force. Nevertheless, the trim values in equation 5.4 resulted in the most realistic open-loop simulation. The open-loop simulation gave reasonable flight behavior (ref. figure 6.2a) matching the theory. The UAV starts with zero speed. As the airplane gain more speed, the lift force increases, and the UAV pitches up. Then the speed reduces and lift is lost. Consequently, the UAV starts to drop again, seen as oscillating behavior. The phugoid mode is almost in the right half-plane resulting in an unstable UAV with very low damping. However, with a faster and damped short-mode, there are acceptable flight characteristics.

Addressing the stability properties of LQR and successive loop closure. In theory, the LQR has the best stability performance, as confirmed in this study. Successive loop closure had considerably larger displaced travel and higher oscillations than LQR relating to moving mass. Also, the gain and phase margin is low when it comes to the PID's capability of controlling moving mass and pitch angle (ref. 5.2). However, by introducing saturation for the LQR controller, one cannot guarantee that the system is stable. One advantage with

SLC is robustness without the ascend/descend reference between altitude hold in figure 5.4. The pitch angle PID controller can be constrained to $|\theta| = 15^\circ$ and prevent stall for a step reference, which is not possible for the LQR. By weighing pitch and pitch rate state, the LQR still increased angle above 15° degrees and the UAV stalled.

The purpose of the CAD was to illustrate some of the challenges of implementing a moving mass actuation for both longitudinal and lateral motion. MMC occupies much internal space for its support stiffeners. Consequently, the fuselage shell must be stiffer to withstand air loads and finite element method (FEM) verifications are necessary to secure a reliable UAV. Another factor is assembly complexity, especially for the moving mass inside the main wing. It is limited space in the wing and challenging to assemble MMC equipment, still ensuring functionality and maintainability. There are advantages and disadvantages of using a stepper motor to move the mobile masses compared to a linear actuator. The linear actuator is more stable than the stepper motor's design because the gear rack and belt of the latter may introduce excessive friction and slack into the system. However, smaller mass and less travel are disadvantages of a linear actuator. With the UAV's own batteries constituting the moving mass, no additional weight is added. However, added wiring and power distribution between the lateral and longitudinal battery must be taken into consideration. Using CAD ensures sensible parameters for the moment of inertia and verifies that the location of the wings is realistic. Based on the completed simulation, one can conclude that the design is not optimal. For instance, the tail could have been shorter since the total movable space in the rear part of the UAV is not utilized. Also, for the given reference generator, the longitudinal moving mass could be smaller. Furthermore, the stepper motor could be fixed at a specific location without being an integrated part of the moving mass, entailing a smaller fuselage. For real testing like Vengate (2016)[19] performed in his study, a UAV with both conventional control surfaces and MMC is necessary in case of malfunction of the moving mass system.

The moment of inertia tensor is assumed to be constant, which is conservative and needs to be discussed further. By changing the location of the longitudinal moving mass from a defined zero point to the rear position, the I_{yy} increased with 68% of the UAV in SolidWorks. Also, the other terms of the inertia tensor changed and affected the mass matrix $\mathbf{M}_{RB}$ and implies that the assumption of a constant I_{yy} is unrealistic.

The simulation is performed on the assumption that no wind, friction or other disturbances are present. Obviously, this cannot be neglected in the real world. Also, sensor noise is assumed to be zero, resulting in a perfect measurement of states. An observer or a Kalman filter must be applied in a real system to filter noise and sensor fusion in order to obtain reliable states.

The original idea was to examine both longitudinal and lateral motion for the UAV with two orthogonal moving masses as shown in figure 5.1. The longitudinal motion was first investigated. Due to problems with the model, this thesis is limited to gaining more insight and understanding of the longitudinal behavior. With the lateral motion removed from the scope, the thesis presents an analytic derived linear model for the longitudinal motion of a

UAV, controlled by an internal moving mass. Moving mass control introduces a new control mechanism compared to conventional control surfaces like ailerons, elevators and rudders. The mechanism is installed internally and protected from ice and erosion. However, the dynamics are highly nonlinear and coupled as inertia tensor changes. Through other studies addressing the same theme, it has been shown that moving masses is most applicable for low speed and high altitude UAVs, i.e. where the density of air is low and traditionally control surfaces lose the level of controllability. Disregarding the high altitude, the same conclusion can be drawn from this study, achieving total control of the UAV at the low cruising speed of 10 m/s. Moreover, MMC can generate enough moment to fly the UAV for a given ascend/descend and altitude hold reference.

7.1 Future Work

In the future, moving mass actuation along the lateral axis must be examined to obtain a completely maneuverable UAV. However, the roll and pitch of a UAV can be controlled with two orthogonal moving masses. For yaw control, either a rudder or differential thrust from two motors mounted on each side of the wing is required.

A recommendation for future work is to look into the Aerospace blockset package in MATLAB and Simulink. The package offers blocks for modeling aerodynamic wing forces and 6 degrees of freedom equations of motion. Also, the package includes mass property blocks meant to estimate the change in the inertia tensor for an aircraft or rocket during the loss of mass due to fuel consumption.

Furthermore, one can build a fixed-wing aerodynamic model with the package for a UAV controlled by conventional control surfaces with the integration of change in inertia tensor. Then a stable UAV flying at constant attitude can be simulated and altering the inertia to see how the system responds. Combining a look-up table with the different inertia tensor terms from CAD software as input to the mass properties blocks, one could find an adequate model for predicting inertia change and integrating it with the aerodynamic model. This could be used to develop a non-linear representation. Furthermore, the Aerospace blockset package contains wind blocks for creating a real-life simulation environment.

Bibliography

[1] R. Oscar vila, "Modelizacion De Aeronaves No Tripuladas Con Simulink," Madrid, 2011.

[2] M. Raffel, F. Wienke, and A. Dillmann, "Flight-testing stability and controllability of otto Lilienthal's monoplane design from 1893," *Journal of Aircraft*, vol. 56, no. 4, pp. 1735–1742, 2019.

[3] P. Gelle, T. Risch, and L. Portes, "CONCRODE - The Supersonic Race," 2017.

[4] R. W. Beard, "Small unmanned aircraft : Theory and practice," Princeton, 2012.

[5] A. Martinsen and J. Frantzen, "Norges største droneoperasjon - droner i lufta i to uker i gjerdrum - uas norway," https://www.uasnorway.no/norges-storste-droneoperasjon-droner-i-lufta-i-to-uker-i-gjerdrum/, January 2021, (Accessed on 02/14/2021).

[6] M. Politovich, "Aircraft icing," in *Encyclopedia of Atmospheric Sciences*, J. R. Holton, Ed. Oxford: Academic Press, 2003, pp. 68–75. [Online]. Available: https://www.sciencedirect.com/science/article/pii/B0122270908000555

[7] K. L. Sørensen, *Autonomous Icing Protection Solution for Small Unmanned Aircraft: An Icing Detection, Anti-Icing and De-Icing Solution, Thesis for the degree of Philosophiae Doctor*. Trondheim: Norwegian University of Science and Technology, Department of Engineering Cybernetics, 2016.

[8] SkyBrary, "In-flight icing - skybrary aviation safety," https://www.skybrary.aero/index.php/In-Flight_Icing, Desember 2020, (Accessed on 02/15/2021).

[9] C. Notebook.net, "Icing in the aviation environment," https://www.cfinotebook.net/notebook/weather-and-atmosphere/icing-in-the-aviation-environment, (Accessed on 05/19/2021).

[10] J. Li, C. Gao, W. Jing, and P. Wei, "Dynamic analysis and control of novel moving mass flight vehicle," *Acta Astronautica*, vol. 131, pp. 36–44, 2 2017.

[11] C. Gao, W. Jing, and P. Wei, "Research on application of single moving mass in the reentry warhead maneuver," *Aerospace Science and Technology*, vol. 30, no. 1, pp. 108–118, 10 2013.

[12] J. Li, S. Chen, C. Li, C. Gao, and W. Jing, "Adaptive control of underactuated flight vehicles with moving mass," *Aerospace Science and Technology*, vol. 85, pp. 75–84, 2 2019.

[13] C. Shao, L. Nie, and W. Chen, "Analysis of weakly ionized ablation plasma flows for a hypersonic vehicle," *Aerospace Science and Technology*, vol. 51, pp. 151–161, 4 2016.

[14] J. H. Wang, L. H. Liu, P. Wang, and G. J. Tang, "Guidance and control system design for hypersonic vehicles in dive phase," *Aerospace Science and Technology*, vol. 53, pp. 47–60, 6 2016.

[15] R. I. Jones, "The design challenge of high altitude long endurance (hale) unmanned aircraft," *The Aeronautical Journal (1968)*, vol. 103, no. 1024, p. 273–280, 1999.

[16] X. Wang, W. Zhou, R. Mu, and Z. Wu, "Modeling and simulation of mass-actuated flexible aircraft for roll control," *Aerospace Science and Technology*, vol. 107, p. 106254, 12 2020.

[17] S. A. Erturk, "Performance Analysis, Dynamic Simulation and Control of Airplane, Mass-Actuated Airplane," Ph.D. dissertation, The University of Texas at Arlington, 2016.

[18] J. Waishek, A. Dogan, and W. Blake, "Derivation of the dynamics equations of receiver aircraft in aerial refueling," *Journal of guidance, control, and dynamics*, vol. 32, no. 2, pp. 586–598, 2009.

[19] S. R. Vengate, *Development and Flight Test of Moving-mass Actuated Unmanned Aerial Vehicle, Master's thesis,*. Texas: The University of Texas at Arlington, 2016.

[20] L. Chen, G. Zhou, X. J. Yan, and D. P. Duan, "Composite control strategy of stratospheric airships with moving masses," *Journal of Aircraft*, vol. 49, no. 3, pp. 794–801, 2012.

[21] J. Li, C. Gao, C. Li, and W. Jing, "A survey on moving mass control technology," *Aerospace Science and Technology*, vol. 82-83, pp. 594–606, 2018. [Online]. Available: https://doi.org/10.1016/j.ast.2018.09.033

[22] T. Haus, M. Orsag, and S. Bogdan, "Design considerations for a large quadrotor with moving mass control," *2016 International Conference on Unmanned Aircraft Systems, ICUAS 2016*, pp. 1327–1334, 2016. [Online]. Available: https://ieeexplore.ieee.org/document/7502680

[23] J. G. Graver, "Underwater Gliders: Dynamics, Control and Design," Ph.D. dissertation, Princeton Univeristy, 2005.

[24] D. W. Childs, “A movable-mass attitude-stabilization system for artificial-gspace stations,” Mechanical Engineering and Applied Mathematics University of Louisville, Kentucky, Tech. Rep., 1972.

[25] J. Virgili-Llop, H. C. Polat, and M. Romano, “Attitude stabilization of spacecraft in very low earth orbit by center-of-mass shifting,” *Frontiers Robotics AI*, vol. 6, no. FEB, pp. 1–19, 2019.

[26] T. L. Edwards and M. H. Kaplan, “Automatic spacecraft detumbling by internal mass motion,” *AIAA Journal*, vol. 12, no. 4, pp. 496–502, 1974.

[27] Q. Zheng and Z. Zhou, “Stability of Moving Mass Control Spinning Missiles with Angular Rate Loops,” 2019. [Online]. Available: https://doi.org/10.1155/2019/7832602

[28] D. McLean, *Automatic flight control systems*, ser. Prentice Hall International series in systems and control engineering. New York: Prentice Hall, 1990.

[29] B. E. Demir, R. Bayir, and F. Duran, “Real-time trajectory tracking of an unmanned aerial vehicle using a self-tuning fuzzy proportional integral derivative controller,” vol. 8, no. 4, pp. 252–268, 2016.

[30] T. I. Fossen, “Mathematical Models for Control of Aircraft and Satellites,” Department of Engineering Cybernetics, Norwegian University of Sience and Technology, Tech. Rep. January, 2011.

[31] T. I. Fossen *HANDBOOK OF MARINE CRAFT HYDRODYNAMICS AND MOTION CONTROL*, 2nd ed. Chichester: John Wiley & Sons, Ltd, 2021.

[32] J. M. B.Eng., “Cessna Skyhawk II / 100 - Performance Assessment,” p. 20, 2003. [Online]. Available: http://www.temporal.com.au/

[33] A. Kulshreshtha, S. K. Gupta, and P. Singhal, “FEM/CFD analysis of wings at different angle of attack,” in *Materials Today: Proceedings*, vol. 26. Elsevier Ltd, 1 2019, pp. 1638–1643.

[34] Matlab, “Continuous-time or discrete-time pid controller - simulink - mathworks nordic,” https://se.mathworks.com/help/simulink/slref/pidcontroller.html, May 2021, (Accessed on 05/11/2021).

Appendix

Appendix A: Matlab Code

Appendix B: Simulink Diagrams

Appendix A

MATLAB Code

A.1 Generate Equation of Motion Script Function

```
%% Template for equation of motion
clear
clc

% Constants
syms rho CL0 CD0 m_plane m S1 S2 g Iy S_prop...
    C_prop K_motor real

% States and control symbolic variable
syms u w q real
syms xt yt theta real
syms delta_m deltaT real

% States and control vector
nu = [u;w;q];
eta = [xt;yt;theta];
cont = [delta_m;deltaT];

% Pos of mean wing
syms p1MW p2MW real
L1 = [1     0    0;
      0     1    0;
     -p2MW  p1MW  1];

% Rotation of mean wing
syms iota1 real
P1 = [cos(iota1)   sin(iota1) 0;
```

```
      -sin(iota1)  cos(iota1) 0;
        0              0      1];

% W_wing of mean wing
K1 = L1*P1;
V_WingMW = K1'*nu;

A1 = simplify(0.5*rho*S1*...
    [-CD0*norm(V_WingMW) CL0*V_WingMW(2)    0;
    -CL0*V_WingMW(2)    -CD0*norm(V_WingMW) 0;
              0                  0          0]);

B1 = L1*P1*A1*P1'*L1';

% Pos of small wing
syms p1SW p2SW real
L2 = [1     0    0;
     0      1    0;
    -p2SW  p1SW  1];

% Rotation of mean wing
syms iota2 real
P2 = [cos(iota2)   sin(iota2) 0;
      -sin(iota2)  cos(iota2) 0;
        0              0      1];
% W_wing of mean wing
K2 = L2*P2;
V_WingSW = K2'*nu;

A2 = simplify(0.5*rho*S2*...
    [-CD0*norm(V_WingSW)   CL0*V_WingSW(2)       0;
       -CL0*V_WingSW(2)   -CD0*norm(V_WingSW)    0;
              0                  0               0]);

B2 = L2*P2*A2*P2'*L2';

% Force act on center of gravity from wings
tau_aero = (B1 + B2)*nu;

% Gravity force on plane
tau_grav = [-m_plane*g*sin(theta);
             m_plane*g*cos(theta);
                      0          ];

% Moving mass element
```

```
tau_mass = g*m*[0;0;-cos(theta)*delta_m];

% Propulse force
tau_prop = 0.5*rho*S_prop*C_prop*...
    [((K_motor*deltaT)^2 - (sqrt(u^2 + w^2))^2);
                          0;
                          0];
% Rigid body matrix
M = [m_plane    0    0;
        0    m_plane 0;
        0       0    Iy];
% coriolis matrix
C = [0   q  0;
     -q  0  0;
     0   0  0];

% Non-linear eqation of motion
nu_dot = M\(-C*nu + tau_aero + tau_grav + tau_mass + tau_prop);
J_long = [Rzyx(0,theta,0)     zeros(3);
             zeros(3)      Tzyx(0,theta)];
eta_dot = J_long([1 3 5],[1 3 5])*nu;

% flip sign for z to h altitude
eta_dot(2,1) = eta_dot(2,1)*-1;

% Linearization and find A, B matrix
f = [nu_dot;eta_dot];
x_stateAll = [u;w;q;xt;yt;theta];
Aall = simplify(jacobian(f,x_stateAll));
Ball = simplify(jacobian(f,cont));

% Add longitudinal moving mass actuation state
syms T real  % Time constant
Ammc = -1/T;
Bmmc =  1/T;
Cmmc = 1;
A12 = Ball*[1 0]';

Atot = [Aall A12;
        zeros(1,6) Ammc];

Btot = [0 Ball(1,2);
        zeros(5,2);
        Bmmc 0];
```

```
% Add integral state for LQR control
gammaRow = [0 0 0 0 1 0 0];
Atot = [Atot;gammaRow];
Atot = [Atot  zeros(8,1)];
Btot = [Btot;0 0];

%Extract A and B matrix for different controllers
Alqr = Atot([1 2 3 5 6 7 8],[1 2 3 5 6 7 8]);
Blqr = Btot([1 2 3 5 5 7 8],[1 2]);

Aslc = Atot([1 2 3 5 6 7],[1 2 3 5 6 7]);
Bslc = Btot([1 2 3 5 5 7],[1 2]);

% Create state space function
x_state = [u;w;q;theta];
matlabFunction(Alqr,Blqr,Aslc,Bslc,'File','SSLinMod'...
    ,'Vars',{rho,CL0,CD0,m_plane,m,S1,S2,g,Iy,p1MW,...
    p2MW,p1SW,p2SW,S_prop,C_prop,K_motor,iota1,...
    iota2,T,x_state,cont});
```

A.2 Parameters and Simulation Script

```
%% Parameters and simulation
clear
clc

% Parameters plane
CD0 = 0.026042;          % Drag coefficent 0
CL0 = 0.307770;          % lift coefficent 0
rho = 1.2682;            % Density of air
S1 = 0.28;               % Area of mean wing
S2 = 0.02;               % Area of small wing
deg2radCon = pi/180;     % Convert between degree and radians
g = 9.81;                % Gravity constant
m_plane = 3.5;           % Mass of plane
m = 0.4;                 % Mass of moving mass
Iy = 0.148;              % Moment of inertia
S_prop = 0.0314;         % Aera of propeller
C_prop = 1;              % Propeller constant
K_motor = 25;            % motor constant
T = 0.1;                 % Time constant

% Saturations parameters
thetaMax = deg2rad(15);  % Max ascending pitch angle
thetaMin = deg2rad(-15); % Max descendig pitch angle
```

```
actMassBack = 0.455;      % Max travel backward for MMC
actMassFront = 0.2;       % Max travel forward for MMC

% Pos of mean wing
p1MW = 0.1;
p2MW = 0.08;
iota1 = 0*deg2radCon;
% Pos of small wing
p1SW = 0.76;
p2SW = 0.01;
iota2 = -4*deg2radCon;    % Negative, since the
                          % wings are defined with
                          % same rotation in the EoM
%% Trim point
alpha = 1;
Va = 10;
deg2radCon = pi/180;

u = Va*cos(alpha*deg2radCon);
w = Va*sin(alpha*deg2radCon);
q = 0;
theta = 0*deg2radCon;

x0_state = [u;w;q;theta];
cont = [0;0.5];

%% State space model
[Alqr,Blqr,Aslc,Bslc] = SSLinMod(rho,CL0,CD0,m_plane,...
    m,S1,S2,g,Iy,p1MW,p2MW,p1SW,p2SW,S_prop,C_prop,...
    K_motor,iota1,iota2,T,x0_state,cont);

Clqr = eye(length(Alqr));
Dlqr = zeros(size(Blqr));

Cslc = eye(length(Aslc));
Dslc = zeros(size(Bslc));

%% Weightning Q and R matrix
uW = 30;
wW = 1;
qW = 120;
hW = 1;
thetaW = 20;
MMCposW = 1;
gammW = 5;
```

```
69
70 Q = diag([uW wW qW hW thetaW MMCposW gammW]);
71
72 % R matrix
73 R = [2 0;
74      0 1];
75
76 % State feedback lqr calculation
77 K = lqr(Alqr,Blqr,Q,R);
78
79 % Reference feedforward
80 F = [K(1,1) K(1,3) K(1,4) K(1,5);
81      K(2,1) K(2,3) K(2,4) K(2,5)];
```

Appendix B

Simulink Diagrams

B.1 Successive Loop Closure

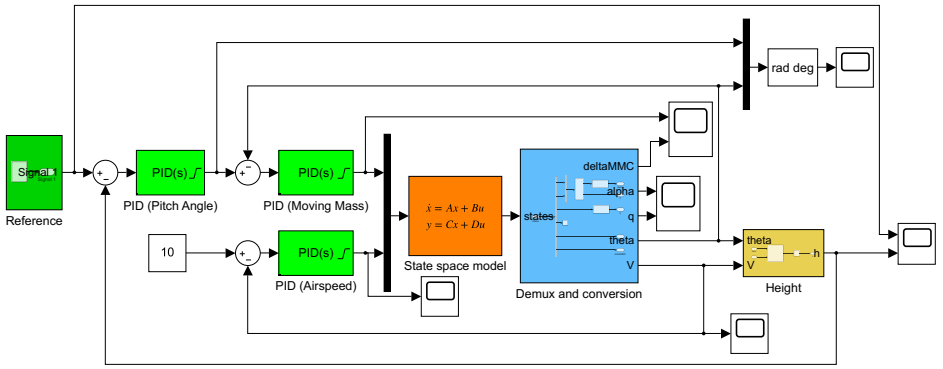

Figure B.1: Overview of Successive loop closure controller design

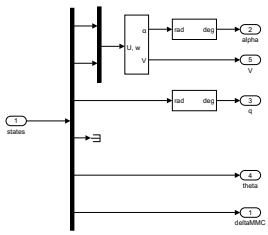

(a) Demux and conversion

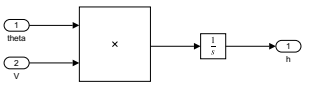

(b) Height

Figure B.2: SLC blocks

B.2 Linear Quadratic Regulator (LQR)

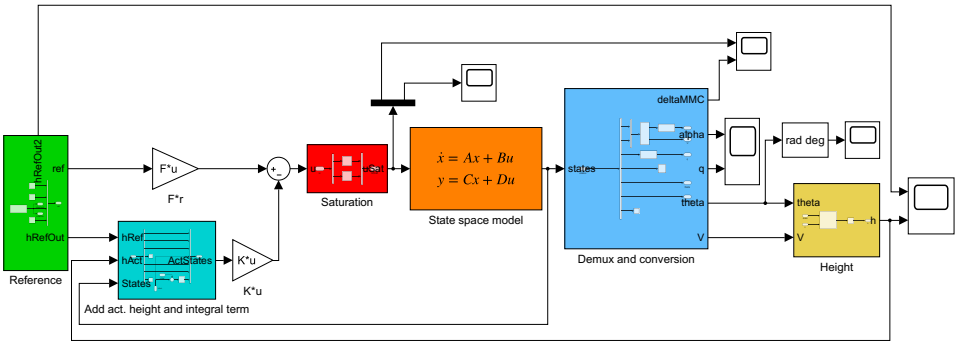

Figure B.3: Overview of LQR controller design

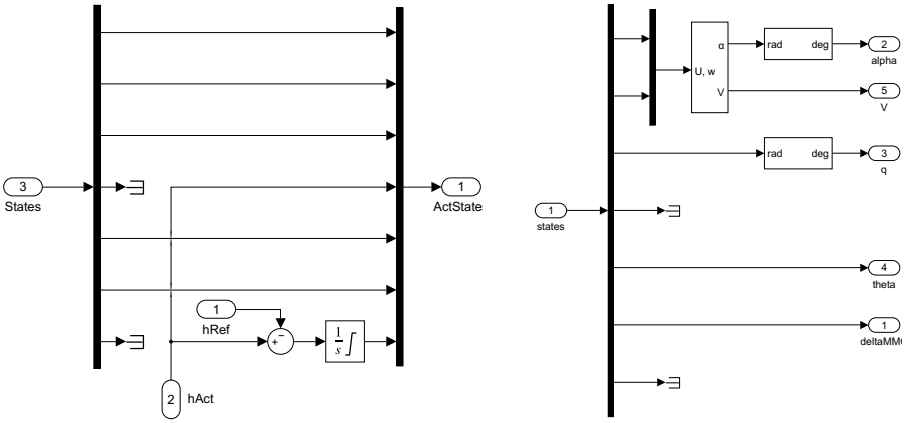

(a) Add height and integral term

(b) Demux and conversion

Figure B.4: LQR blocks

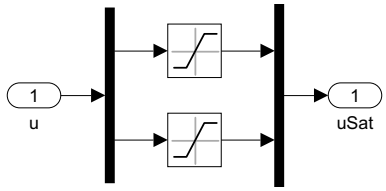

Figure B.5: Saturation block

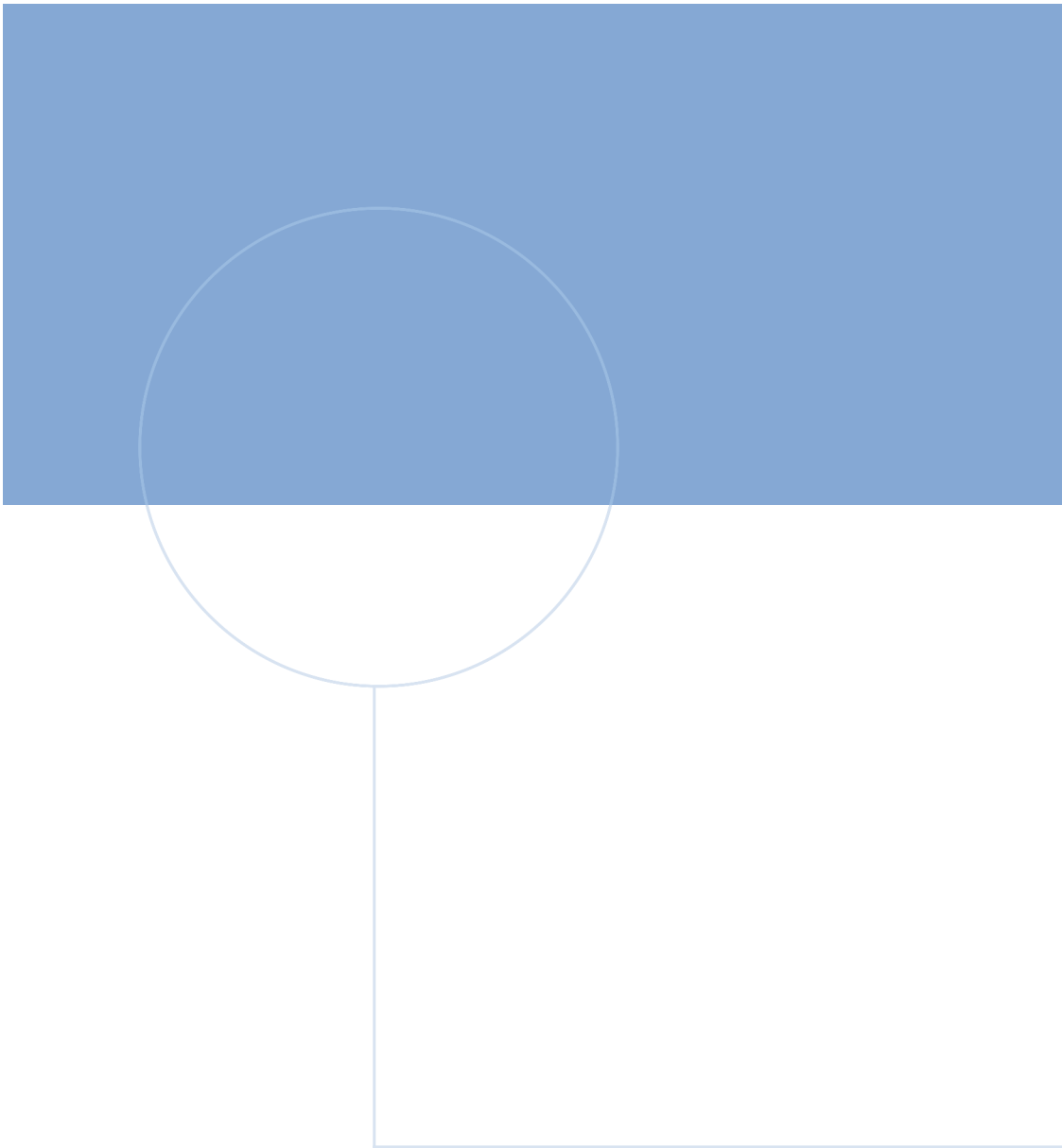

NTNU

Norwegian University of
Science and Technology